

ACCEPTED VERSION

R. Tamblyn, M. Hand, L. Morrissey, T. Zack, G. Phillips, D. Och
Resubduction of lawsonite eclogite within a serpentinite-filled subduction channel
Contributions to Mineralogy and Petrology, 2020; 175(8):1-22

© Springer-Verlag GmbH Germany, part of Springer Nature 2020

*This is a post-peer-review, pre-copyedit version of an article published in **Contributions to Mineralogy and Petrology**, The final authenticated version is available online at:*
<http://dx.doi.org/10.1007/s00410-020-01712-1>

PERMISSIONS

<https://www.springer.com/gp/open-access/publication-policies/self-archiving-policy>

Self-archiving for articles in subscription-based journals

Springer journals' [policy on preprint sharing](#).

By signing the Copyright Transfer Statement you still retain substantial rights, such as self-archiving:

*Author(s) are permitted to self-archive a pre-print and an author's **accepted manuscript** version of their Article.*

.....

b. An Author's Accepted Manuscript (AAM) is the version accepted for publication in a journal following peer review but prior to copyediting and typesetting that can be made available under the following conditions:

(i) Author(s) retain the right to make an AAM of their Article available on their own personal, self-maintained website immediately on acceptance,

(ii) Author(s) retain the right to make an AAM of their Article available for public release on any of the following 12 months after first publication ("Embargo Period"): their employer's internal website; their institutional and/or funder repositories. AAMs may also be deposited in such repositories immediately on acceptance, provided that they are not made publicly available until after the Embargo Period.

An acknowledgement in the following form should be included, together with a link to the published version on the publisher's website: "This is a post-peer-review, pre-copyedit version of an article published in [insert journal title]. The final authenticated version is available online at: [http://dx.doi.org/\[insert DOI\]](http://dx.doi.org/[insert DOI])".

When publishing an article in a subscription journal, without open access, authors sign the Copyright Transfer Statement (CTS) which also details Springer's self-archiving policy.

See Springer Nature [terms of reuse](#) for archived author accepted manuscripts (AAMs) of subscription articles.

2 September 2021

<http://hdl.handle.net/2440/128444>

[Click here to view linked References](#)

1 Resubduction of lawsonite eclogite within a serpentinite-filled subduction channel

2 Tamblyn, R.^{1*}, Hand, M.¹, Morrissey, L.², Zack, T.^{1,3}, Phillips, G.⁴, Och, D.⁵

3
4 ¹ Department of Earth Sciences, The University of Adelaide, Adelaide, Australia

5
6 ² School of Natural and Built Environments, The University of South Australia, Adelaide, Australia

7
8 ³ Department of Earth Sciences, University of Gothenburg, Gothenburg, Sweden

9
10 ⁴ Geological Survey of New South Wales, Sydney, Australia

11
12 ⁵ WSP Parsons Brinckerhoff, Sydney, Australia

13
14 * Corresponding author: renee.tamblyn@adelaide.edu.au

15
16
17

18 **Abstract**

19
20 Translating burial and exhumation histories from the petrological and geochronological
21 record of high-pressure assemblages in subduction channels is key to understanding subduction
22 channel processes. Convective return flow, either serpentinite or sediment hosted, has been suggested
23 as a potential mechanism to retrieve rocks from significant depths and exhume them. Numerical
24 modelling predicts that during convective flow, subducted material can be cycled within a
25 serpentinite-filled subduction channel. Geochronological and petrological evidence for such cycling
26 during subduction is preserved in lawsonite eclogite from serpentinite mélangé in the Southern New
27 England Orogen, eastern Australia. Ar–Ar, Rb–Sr phengite and U–Pb titanite geochronology,
28 supported by phase equilibrium forward modelling and mineral zoning, suggest Cambro-Ordovician
29 eclogite underwent two stages of burial separated by a stage of partial exhumation. The initial
30 subduction of the eclogite at ca. 490 Ma formed porphyroblastic prograde-zoned garnet and lawsonite
31 at approximate P – T conditions of at least 2.9 GPa and 600 °C. Partial exhumation to at least 2.0 GPa
32 and 500 °C is recorded by garnet dissolution. Reburial of the eclogite resulted in growth of new Mg-
33 rich garnet rims, growth of new prograde-zoned phengite and recrystallization of titanite at P – T
34 conditions of approximately 2.7 GPa and 590 °C. U–Pb titanite, and Ar–Ar and Rb–Sr phengite ages
35 constrain the timing of reburial to ca. 450 Ma. This was followed by a second exhumation event at
36 approximately 1.9 GPa and 520 °C. These conditions fall along a cold approximate geotherm of 230
37 °C/GPa. The inferred changes in pressure suggest the lawsonite eclogite underwent depth cycling
38 within the subduction channel. Geochronological data indicates that partial exhumation and reburial
39
40
41
42
43
44
45
46
47
48
49
50
51
52
53
54
55
56
57
58
59
60
61
62
63
64
65

1
2 30 occurred over ca. 50 M.y., providing some estimation on the timescales of material convective cycling
3 31 in the subduction channel.

4 32

5
6 33 *Keywords:* eclogite, lawsonite, resubduction, high-pressure, corner flow, serpentinite
7
8 34

9
10 35

11 36 **1. INTRODUCTION**

12
13 37 Metamorphism along cool geothermal gradients in subduction zones produces eclogite-facies
14
15 38 mineral assemblages. These assemblages often preserve an abundance of prograde, peak and
16
17 39 retrograde petrological relationships. For example, elemental zoning in garnet and micas can be
18
19 40 preserved due to slow rates of diffusion, and temperature-sensitive minerals such as lawsonite can
20
21 41 also be preserved (Tsuji-mori et al., 2006; Tsuji-mori & Ernst, 2014). Given this potential to preserve
22
23 42 extensive petrological relationship histories, methods such as phase equilibrium modelling coupled
24
25 43 with new and emerging geochronological techniques open avenues to explore the pressure–
26
27 44 temperature–time (P – T – t) histories of these high-pressure low-temperature assemblages, and make
28
29 45 inferences about the behaviour of the subduction systems that host them.
30
31 46

32
33
34
35
36
37 47 The application of sophisticated petrological techniques to eclogite and blueschist assemblages
38
39 48 has highlighted the potential for complex P – T – t histories. This is particularly apparent in serpentinite
40
41 49 mélanges. Mixing, accumulation, long-lived residence and intrachannel circulation of high-pressure
42
43 50 lithologies have started to emerge as common phenomena within subduction channels (e.g. Krebs et
44
45 51 al., 2008; Lázaro et al., 2009). Numerical modelling has sought to explain the dynamics of material
46
47 52 within subduction channels, and has demonstrated that complex P – T – t histories are possible, arising
48
49 53 from cycling and corner flow within the channel (Gerya et al, 2002, Stöckhert & Gerya, 2005; Roda et
50
51 54 al., 2019). Examples of high-pressure rocks that have seen two or more cycles of burial have been
52
53 55 recognised through geochronological and mineralogical evidence, for example, dating zones within
54
55 56 metamorphic zircon (e.g. Liati et al., 2016). However, in lieu of such useful petrochronological
56
57 57 methods, recognising multiple burial cycles can prove difficult.
58
59
60
61
62
63
64
65

58

1
2 59 Lawsonite eclogite is globally rare, despite the range of bulk compositions that support the
3
4 60 formation of lawsonite-garnet-omphacite (Wei & Clarke, 2011). Therefore, their occurrence probably
5
6 61 reflects unusually good preservation of deeply buried, cold subducted material. Consequently,
7
8 62 lawsonite eclogites potentially preserve comprehensive records of the physical conditions of
9
10 63 subduction channels. This study presents detailed petrological results from eclogite in the Southern
11
12 64 New England Orogen (SNEO), that supports partial exhumation and reburial of a single block of
13
14 65 lawsonite eclogite during on-going subduction. Phase diagrams constrain the approximate pressure–
15
16 66 temperature (P – T) conditions of partial exhumation and reburial within the subduction channel, which
17
18 67 is supported by U–Pb titanite, and Rb–Sr and Ar–Ar phengite geochronological data. The cycle of
19
20 68 exhumation and reburial records an approximate total pressure and temperature fluctuation of at least
21
22 69 1.6 GPa and 190 °C and is constrained to have occurred over ca. 50 M.y.. If the pressure fluctuations
23
24 70 recorded by high-pressure mineral assemblages reflect oscillations in burial depths, such records
25
26 71 support the notion of convective flow within the subduction channel.
27
28
29
30

31 72

32 33 73 **2. GEOLOGICAL SETTING**

34
35 74

36 37 75 **2.1 The Southern New England Orogen**

38
39 76 The Southern New England Orogen (SNEO) in eastern Australia is the youngest and most
40
41 77 outboard orogen of the Tasmanides (Fig. 1a; Kemp et al., 2009; Glen, 2013; Phillips et al., 2015). The
42
43 78 Tasmanides are interpreted to have formed as a result of long-lived subduction on the East
44
45 79 Gondwanan margin during the Cambrian–Triassic, which resulted in a series of eastwards-younging
46
47 80 orogens. The oldest and most westerly of these is the Delamerian Orogen, which formed at ca. 515–
48
49 81 490 Ma on the margin of cratonic Australia, and was post-dated by the Lachlan-Thompson Orogen at
50
51 82 ca. 484–340 Ma (Fig. 1a). The SNEO formed between the upper Devonian-Triassic, and consists of a
52
53 83 volcanic arc, forearc basin and accretionary complex (Fig. 1b; Jenkins et al., 2002; Jessop et al.,
54
55 84 2019). The Devonian-Carboniferous volcanic arc outcrops, but is generally obscured under the
56
57 85 younger Permian-Triassic Sydney-Gunnedah basin (Jenkins et al., 2002). The Tamworth Belt contains
58
59
60
61
62
63
64
65

1
2
3
4
5
6
7
8
9
10
11
12
13
14
15
16
17
18
19
20
21
22
23
24
25
26
27
28
29
30
31
32
33
34
35
36
37
38
39
40
41
42
43
44
45
46
47
48
49
50
51
52
53
54
55
56
57
58
59
60
61
62
63
64
65

86 a forearc basin, consisting of felsic volcanic rocks and volcanoclastics (Roberts & James, 2010). The
87 Tablelands Complex consists of deformed sediments and oceanic basalt that accumulated within an
88 accretionary complex. These are separated by the serpentinite-bearing Peel Manning Fault System
89 (Fig. 1b). The SNEO also contains numerous felsic magmatic rocks of the Permian-Triassic New
90 England Batholith, which intrude the Tablelands Complex and the Early Permian basins (Leitch,
91 1975; Shaw and Flood, 1981; Phillips et al., 2011). These are interpreted to have formed as the orogen
92 evolved from an accretionary system to a back-arc position (Jenkins et al., 2002; Phillips et al., 2011).

93 94 **2.2 Tectonic framework of the high-pressure rocks and the Tasmanides**

95 There has been significant debate surrounding the evolution of the Tasmanides, including the
96 tectonic significance of the high-pressure rocks. Notably, all the geochronology reported from
97 serpentinite-hosted high-pressure exotic blocks in the SNEO is significantly older than the enclosing
98 geology (Fig. 1b; e.g. Fukui et al., 1995, Sano et al., 2004; Phillips et al., 2015; Manton et al., 2017;
99 Tamblyn et al., 2019a). The most coherent views about the evolution of the Tasmanides involve
100 eastward retreat of a subduction system that formed close to the cratonic margin during the mid-late
101 Cambrian (e.g. Collins, 2002; Phillips & Offler, 2011; Moresi et al., 2014; Phillips et al., 2015). The
102 general consensus is the high-pressure rocks found in the SNEO were formed in a subduction channel
103 on the cratonic margin of Australia during the Delamerian Orogen in the Cambrian–Ordovician.
104 Subsequent cooling and transport of the high-pressure rocks occurred during eastward-directed slab
105 rollback, until the high-pressure rocks were exhumed in their current location in the Permian-Triassic
106 SNEO (Phillips & Offler, 2011; Phillips et al., 2015; Tamblyn et al., 2019a). During this rollback, the
107 Lachlan/Thompson Orogens developed in a backarc setting on the upper plate (e.g. Collins, 2002;
108 Kemp et al., 2009; Moresi et al., 2014). Eastward younging arcs track the rollback of the subduction
109 zone, accompanied by voluminous I and S-type magmatism formed from arc and back-arc rifting
110 processes (Collins, 2002; Collins & Richards, 2008). This eastward migration is also revealed in ϵ_{Nd}
111 isotopes of magmatic rocks, which demonstrate an increasingly juvenile signature as the subduction
112 zone migrated away from the cratonic margin (Kemp et al., 2009).

114 2.3 High-pressure metamorphism and mélangé formation in the SNEO

1 High-pressure metamorphic rocks hosted in serpentinite occur throughout the SNEO at Attunga,
2
3
4 116 Gleneden, Glenrock, Pigna Barney and Port Macquarie (Fig. 1b; Phillips et al., 2015). The Port
5
6 117 Macquarie mélangé contains by far the largest lithological variety of high pressure-rocks, which are
7
8 118 described in detail by Och et al. (2003; 2007) and Tamblyn et al. (2019a). The mélangé consists of
9
10 119 exotic high-pressure blocks encased in chlorite-actinolite schist, which is in turn encased within
11
12 120 serpentinite (Fig. 1c). These exotic blocks consist of variably metamorphosed omphacite, low-grade
13
14 121 basaltic rocks, sedimentary rocks, marble, blueschist facies rocks, retrogressed eclogite and lawsonite-
15
16 122 bearing eclogite. In-situ U–Pb geochronology on micro-zircon from the lawsonite eclogite returned a
17
18 123 range of ages from ca. 560–440 Ma (Tamblyn et al., 2019a). The zircons occur as inclusions in garnet
19
20 124 and also occur in the surrounding matrix. Lu–Hf geochronology on lawsonite porphyroblasts gives an
21
22 125 age of 506 ± 15 Ma, and a Lu–Hf garnet-whole rock isochron gives an age of 489.7 ± 5 Ma. These
23
24 126 ages are interpreted to date prograde metamorphism, as garnet cores are enriched in Lu compared to
25
26 127 rims, biasing the age to early garnet growth. Pressure-temperature conditions obtained from phase
27
28 128 equilibrium modelling are approximately 2.7 GPa and 590 °C for the lawsonite eclogite, and 2.0 GPa
29
30 129 and 550 °C for a garnet-omphacite-bearing blueschist block within the same mélangé. Lu–Hf, Sm–
31
32 130 Nd, K–Ar and Ar–Ar ages from adjacent blueschist blocks and fuchsite in serpentinite give ages
33
34 131 between ca. 472 and 420 Ma (Fukui et al., 1995; Och et al., 2010; Tamblyn et al., 2019a). This
35
36 132 geochronology, along with the presence of low-grade sedimentary blocks, confirms the accumulation
37
38 133 of rocks with different P – T histories in the mélangé.
39
40
41
42
43
44
45

134

135 3. PETROGRAPHY

136 Mineralogy of the lawsonite eclogite block (sample RB11) has been described in detail by
137
138 Tamblyn et al. (2019a) and Och et al. (2003; 2007). The eclogite contains porphyroblastic garnet,
139
140 lawsonite and omphacite, in a well-foliated matrix dominated by phengite and containing minor
141
142 titanite (Fig. 2). However, it is clear from optical petrography and elemental mapping that there are
143
144 two distinct mineral assemblages recorded in the sample, summarized in Supplementary Table 1,
145
146 which are referred to as stage 1 and stage 2. Garnet is euhedral and forms crystals up to 7 mm in
147
148
149
150
151
152
153
154
155
156
157
158
159
160
161
162
163
164
165

142 diameter, which have red-coloured cores and paler rims, referred to as garnet 1 and garnet 2
143 respectively (Fig. 2a-d). The inclusion relationships in garnet are summarised in Supplementary
144 Figure 1. Garnet 1 has inclusion-rich cores which contain lawsonite, titanite, omphacite, phengite,
145 glaucophane, chlorite, epidote, stilpnomelane, quartz and zircon (Supp. Fig. 1). Very rarely, quartz
146 inclusions in the outermost part of garnet 1 are surrounded by prominent radial fractures, suggesting
147 the possibility that they were once coesite (Fig. 2e). Garnet 2 forms as ~ 400 µm wide rims on garnet
148 1 that contain chlorite, glaucophane, titanite, omphacite, lawsonite, quartz and zircon (Fig. 2d), and in
149 some instances overgrow matrix phengite. Enclosed inclusions of chlorite, phengite, omphacite,
150 quartz, titanite and pyrite occur at the boundary between garnet 1 and 2 (Supp. Fig. 1). Sigmoidal
151 inclusion trails of titanite are also commonly truncated at the boundary between garnet 1 and garnet 2,
152 with the trails forming at a high angle to the matrix foliation (Supp. Fig. 1). Titanite included in garnet
153 2 is coarser-grained than in garnet 1. Lawsonite forms euhedral crystals up to 3 mm (Fig. 2b,f). It has
154 darker sections containing abundant fine-grained inclusions and clearer sections with coarser-grained
155 inclusions. The inclusions are predominately titanite, epidote, glaucophane and phengite. In places the
156 lawsonite grain boundaries are mantled by small garnet grains, which have been overgrown by a
157 second generation of lawsonite. In other places the clearer lawsonite occurs as an overgrowth on
158 darker lawsonite crystals (Fig. 2f). The darker, older lawsonite is referred to as lawsonite 1 and the
159 clearer overgrowths are referred to as lawsonite 2. The foliated matrix is part of the stage 2 mineral
160 assemblage, and is defined by coarse phengite (up to 1 mm but commonly ~ 300 µm) and pervasive
161 but modally minor titanite (< 100 µm; Fig. 2b,d). The latter is associated with fine grained allanite
162 and zircon (< 20 µm). Titanite and phengite are coarser in the matrix relative to the inclusions in
163 garnet cores, and in places titanite forms aggregates of grains that rim phengite grains. Omphacite
164 forms monominerallic patches up to 10 mm which are partially replaced by glaucophane and chlorite,
165 as well as relic fractured porphyroblasts up to ~ 500 µm in size (Fig. 2a,b). Omphacite is partially
166 replaced by chlorite and glaucophane. Garnet is partially replaced by chlorite along its grain
167 boundaries or along fractures which cross-cut the garnet (Fig. 2c; Supp. Fig. 1). Where retrograde
168 chlorite occurs with lawsonite, lawsonite is euhedral and unretrogressed, suggesting it was stable
169 during the retrogression of the eclogite. In the matrix, glaucophane also forms foliated euhedral

170 crystals (Fig. 2c). These crystals, as well as coarse titanite crystals, are overgrown by stage 2
171 lawsonite rims. These petrological observations denote two distinct stages of peak metamorphism in
172 the eclogite, separated by a period of retrogression. A schematic representation of the petrologic
173 observations made from optical petrography, phase mapping and elemental mapping can be found in
174 Figure 3.

176 4. METHODS

178 4.1 Electron Probe Micro Analyses and mapping

179 Spot analyses on minerals were obtained using a Cameca SX-5 microprobe at Adelaide
180 Microscopy, using an accelerating voltage of 15 kV and a beam current of 20 nA. Element maps used
181 an accelerating voltage of 15 kV and a 200 nA beam current, Ca, Fe, Mn and Mg were mapped using
182 Wavelength Dispersive Spectrometers (WDS), whereas Al, Si, Ti, K and Na were mapped using
183 Energy Dispersive Spectrometry (EDS). Maps were colour scaled in ImageJ.

185 4.2 Phase equilibrium forward modelling

186 Full phase equilibrium modelling methods are in Supplementary File 1. The rock composition
187 was calculated for the lawsonite eclogite by combining modal proportions of each mineral with its
188 measured chemical composition (Supp. Table 2; 3). Thin sections were mapped with a Quanta600
189 scanning electron microscope (SEM) with mineral liberation analysis (MLA) software to calculate
190 modal proportions of minerals.

191
192 The phase equilibrium models were calculated using THERMOCALC (TC340i) using the
193 internally-consistent thermodynamic dataset 'ds5' (filename tc-ds55.txt; November 2003 updated
194 version of the Holland & Powell, 1998 data set) and activity–composition ($a-x$) models (Supp. Table
195 4; Holland & Powell, 1988; Holland & Powell, 2003; White et al., 2007; Green et al., 2007; Holland
196 & Powell, 2011; Diener et al., 2012) in the chemical system NCKFMASHO. A model for the local
197 rock composition was calculated with water in excess, and a model for the local rock composition was

198 calculated with a set water content, derived from the abundance of hydrous minerals (Supp. Table 2;
199 3).

200

201 **4.3 U–Pb titanite geochronology**

202 Titanite grains were analysed in-situ for U–Pb isotopes using an ASI m50 LA–ICP with an
203 attached 7700 MS at Adelaide Microscopy. Grains were ablated using a spot size of 51 μm , a
204 frequency of 5 Hz, and a surface energy density of 3.5 Jcm^{-2} , with an acquisition time of 80 s for each
205 analysis including 30 s of background measurement and 50 s of ablation. The primary reference
206 titanite MKED-1 was used to correct for elemental fractionation, mass bias and instrument drift over
207 the courses of analyses (Spandler et al., 2016), and a titanite grain from Mt Painter with an age of
208 442.6 ± 1.8 Ma (Elburg et al., 2003) was used as the secondary standard. Corrections were done using
209 the software Iolite (Paton et al., 2011) and age calculations were done using IsoplotR (Vermeesch,
210 2018). The secondary standard from Mt Painter returned a weighted mean $^{206}\text{Pb}/^{238}\text{U}$ age of $440.3 \pm$
211 2.5 Ma (MSWD = 1.5, $n = 22$) throughout the course of the analyses.

212

213 **4.4 Ar–Ar phengite geochronology**

214 Phengite $^{40}\text{Ar}/^{39}\text{Ar}$ isotope analyses utilized conventional furnace step-heating techniques at
215 the University of Melbourne, after the analytical procedures of Phillips et al. (2007). Phengite grains
216 were selected from mineral separates. Due to the possibility of contamination by excess argon in high-
217 pressure rocks (Kelley, 2002), a two-increment step-heating laser approach was employed on single
218 grains of phengite. The laser analyses were conducted at The University of Melbourne, employing the
219 analytical procedures described by Phillips and Harris (2008). This approach was used to screen for
220 any significant intrasample inconsistency in argon content that could be an artefact of (i) multiple
221 generations of phengite growth or (ii) varied amounts of isotopic resetting or excess argon
222 contamination within single grains. Using the single-grain laser approach, spurious isotopic results
223 from a single-grain analysis can be removed from the mean age calculations, using Isoplot software
224 (Ludwig, 2003).

225

226

4.5 Rb–Sr phengite geochronology

227

Phengite was analysed in-situ for Rb and Sr isotopes and major and trace elements using an

228

ESI 213 NWR (TwoVol2) laser ablation system with an attached Agilent 8800QQQ ICP-MS/MS in

229

the Microgeochemistry Laboratory at the University of Gothenburg, Sweden, following the methods

230

of Zack & Hogmalm (2016) and Hogmalm et al. (2017). Full methods are in Supplementary File 1.

231

Laser parameters were a fluence of $\sim 6 \text{ Jcm}^{-2}$ and a frequency of 10 Hz. Phengite was analysed with a

232

spot size of 40 μm , both perpendicular and parallel to cleavage. Titanite was also analysed to obtain

233

initial $^{87}\text{Sr}/^{86}\text{Sr}$ ratios, with a spot size of 50 μm . The primary standard for $^{87}\text{Rb}/^{86}\text{Sr}$ calibration was a

234

pressed nanopowder MicaMg ($^{87}\text{Rb}/^{86}\text{Sr}$ ratio of 154.6; Hogmalm et al., 2017). Other primary

235

standards for $^{87}\text{Sr}/^{86}\text{Sr}$ ratios were the synthetic glass NIST610 ($^{87}\text{Sr}/^{86}\text{Sr}$ ratio: 0.709699; Woodhead

236

& Hergt, 2001) and the natural basaltic glass BCR2G ($^{87}\text{Sr}/^{86}\text{Sr}$ ratio: 0.705003; Elburg et al., 2005).

237

Secondary standards included La Posta biotite grains, with Rb–Sr isochron age of $91.6 \pm 1.2 \text{ Ma}$ and

238

an initial $^{87}\text{Sr}/^{86}\text{Sr}$ ratio of 0.7049 ± 5 (Zack & Hogmalm, 2016), and MDC biotite grains with an

239

isochron age of $519.4 \pm 6.5 \text{ Ma}$ and an initial $^{87}\text{Sr}/^{86}\text{Sr}$ ratio of 0.72 ± 0.002 (unpublished data). Over

240

the course of the analyses, La Posta grains returned an isochron age of $90.5 \pm 4.2 \text{ Ma}$, and MDC

241

grains returned an isochron age of $501.2 \pm 7.2 \text{ Ma}$.

242

243

4.6 LA–ICP–QQQ mapping

244

Phengite was mapped in-situ for Rb and Sr using an ASI m50 LA–ICP–MS with attached

245

Agilent 8800 triple quadrupole MS at Adelaide Microscopy, Australia. The reaction gas used was O_2 ,

246

with laser parameters of a fluence of 7 Jcm^{-2} and a frequency of 10 Hz. The primary standard used

247

was a pressed nanopowder MicaMg, and NIST610 was used as a secondary glass standard. The maps

248

were processed in Iolite (Paton et al., 2011). Results of the mapping are semi-quantitative, and are

249

presented in counts per second (CPS).

250

251

5. RESULTS

252

253 **5.1 Electron Probe Micro Analyses and mapping**

1
2 254 Mineral compositions and end member proportions are reported in Supplementary Table 2
3
4 255 and Tamblyn et al. (2019a), additional phengite, chlorite, omphacite and glaucophane compositional
5
6 256 data is in Supplementary Table 5.
7

8
9 257
10
11 258 EPMA traverses and mapping of whole garnet grains (Fig. 4; 5; Supp. Fig. 2) show complex
12
13 259 zoning in the major elements. In garnet 1, cores show a bell-shaped Mn enrichment, consistent with
14
15 260 prograde zoning (Fig. 4a; 5a). In the outer part of garnet 1 and prominently in garnet 2 there is a series
16
17 261 of thin concentric Mn-rich rings or oscillations (Fig. 5b-c). These narrow Mn-rich zones are often
18
19 262 regular, forming hexagonal garnet crystal shapes (Fig. 5c), but can also be highly irregular, appearing
20
21 263 to form on embayments in the garnet crystal (Fig. 5b). There is an overall average increase in Mn
22
23 264 content from the outer part of garnet 1 to the garnet 2 rim (Fig. 4b). The grossular content of the entire
24
25 265 garnet increases slightly from core to rim, from 0.23 to 0.3, and also shows slight enrichments in thin
26
27 266 concentric rings in the outer garnet that are correlated with the patterns exhibited by Mn (Fig. 5).
28
29 267 Garnet 1 has almandine-poor cores (0.45) increasing to higher almandine content in the outer garnet
30
31 268 (0.65; Fig. 4a), with the exception of slight almandine-poor concentric rings which correlate with the
32
33 269 Mn-rich rings. Garnet 2 is slightly depleted in almandine (Fig. 4b). Pyrope contents are low in garnet
34
35 270 1, ~0.03, with the innermost core showing a very slight depletion compared to the rest of the garnet
36
37 271 (Fig. 5a). Garnet 2 shows distinct step increase in pyrope (0.06) that defines an outer rim ~ 200 μm in
38
39 272 width (Fig. 4b).
40
41
42
43
44
45

46 273
47 274 High resolution EPMA maps (Fig. 5b-c) reveal that garnet 2 forms on a regular to irregular-
48
49 275 shaped original surface of the garnet, as indicated by the white dashed line. The growth of garnet 2 is
50
51 276 marked by a sharp increase in Mn, followed by several variations in Mn, and a final Mn-poor rim
52
53 277 which has been partially replaced by chlorite. Notably, these Mn zoning patterns only correspond to
54
55 278 slight changes in MnO (<0.5 wt%). Fe is slightly depleted in garnet 2. This outer-rim transition is also
56
57 279 marked by a sharp increase in Mg. The oscillations in Mn commonly correlate with slight increases in
58
59 280 Ca.
60
61
62
63
64
65

281

1
2 282 EPMA X-ray maps were also obtained from phengite grains in the matrix and in garnet (Fig.
3
4 283 6; Supp. Fig. 3). Matrix phengites display cores that are depleted in Fe, enriched in Al and slightly
5
6 284 enriched in Na, surrounded by a rim enriched in Si, with enriched Fe and slight enrichment in Mg
7
8 285 (Fig. 6). Phengite grains in garnet show phengite included in garnet 1 is enriched in Si, Mg and Fe,
9
10 286 and depleted in Al and Na (Fig. 6). Phengite included in garnet 2 is enriched in Al and Na, and
11
12 287 depleted in Si and Fe with a slight depletion in Mg, similar to cores of phengite grains in the matrix
13
14 288 (Fig. 6). Compositional zoning in the phengite is sharp and well defined. Overall, the phengite zoning
15
16 289 is defined by an increase in celadonite proportion from core (40%) to outer rim (45%), accompanied
17
18 290 by a decrease in X_{Mg} (0.71–0.63) and an increase in Si (3.43–3.56 p.f.u.; Fig. 7).
19
20
21

22 291

23
24 292 Omphacite occurs as inclusions in garnet 1 and garnet 2, and as coarser grains in the matrix,
25
26 293 which show subtle differences in composition (Fig. 7). Omphacite in the matrix and as inclusions in
27
28 294 garnet 1 is generally 0.37–0.44 proportion jadeite, 0.36–0.43 proportion diopside, 0.08–0.19
29
30 295 proportion hedenbergite with a minor acmite component. Omphacite as inclusions in garnet 2 is
31
32 296 similar in composition, with the exception of occasional diopsodic grains, which are 0.15–0.23
33
34 297 proportion jadeite, 0.47–0.50 proportion diopside, and 0.19–0.26 proportion hedenbergite. Coarse
35
36 298 grains in the matrix and as inclusions in garnet 2 are subtly zoned in X_{Fe} , from ~ 0.27 in the core to ~
37
38 299 0.23 in the rim (Supp. Fig. 4). Inclusions in garnet 1 have an average X_{Fe} of 0.28, and inclusions in
39
40 300 garnet 2 have an average X_{Fe} of 0.3.
41
42
43

44 301

45
46 302 Chlorite forms grains in the matrix that break down garnet and omphacite, along fractures
47
48 303 which cross-cut garnet, and as inclusions at the boundary between garnet 1 and garnet 2 (Supp. Fig.
49
50 304 1). Chlorite as inclusions between garnet 1 and garnet 2 has an average X_{Mg} of 0.46 (Supp. Table 5). It
51
52 305 shows elevated MnO contents compared to the adjacent garnet (0.54–0.73 wt%). Chlorite throughout
53
54 306 the matrix has an average X_{Mg} of 0.38. EPMA X-ray maps show that chlorite is often zoned or patchy
55
56 307 in composition (Supp. Fig. 5).
57
58
59

60 308

61
62
63
64
65

309 Retrograde amphibole is ferro-glaucophane in composition after the nomenclature of Leake et
1 al. (1997), and also shows sharply defined compositional zonation (Supp. Fig. 6). X_{Mg} increases from
2 310 core to rim, accompanied by a slight decrease in Al (1.72–1.39 p.f.u.). There is a slight enrichment of
3 311 Ca in the cores of the glaucophane (0.17 p.f.u.), however, the grains are dominantly sodic. Some
4 312 grains have thin outer rims with slight enrichment in MnO (0.14–0.27 wt%, Supp. Fig. 6).
5 313

10 314
11 315 Titanite differs slightly from ideal formula, with incorporation of Al_2O_3 (up to 2.27 wt%),
12 316 FeO (up to 0.66 wt%) and F (up to 0.6 wt%) into its crystal structure (Supp. Table 5). Al_2O_3 , FeO and
13 317 F contents show positive correlations (Fig. 7).
14 318

21 319 **5.2 Phase equilibrium forward modelling**

22 320 The results of the phase equilibrium forward modelling and corresponding mineral modal and
23 321 compositional isopleths are shown in Figures 8, 9 and 10. Figure 8 shows the phase equilibrium
24 322 model for the total bulk rock composition after Tamblyn et al. (2019a). Figure 9 shows the phase
25 323 equilibrium model for the local rock composition with water in excess, and garnet 1 and lawsonite 1
26 324 removed. This was done to simulate the effective local composition for the stage 2 mineral
27 325 assemblage, as garnet 1 and lawsonite 1 were chemically isolated from the reactive rock composition
28 326 (e.g. Spear, 1988; Marmo et al., 2002; Evans, 2004; Gaides et al., 2008; Konrad-Schmolke et al.,
29 327 2008; Lanari & Engi, 2017). Figure 10 shows the phase equilibrium model with garnet 1 and
30 328 lawsonite 1 removed, but with a set water content, calculated from the modes of hydrous minerals
31 329 ($H_2O = 4.65$ wt%). This was done as the current water content in the rock is most likely a measure of
32 330 the minimum amount of water available in the local rock composition. Figures 11 and 12 can only be
33 331 used for the mineral relations during the secondary assemblage formation after garnet 1 and lawsonite
34 332 1 have been formed. It is likely that the local rock composition had a water content between that
35 333 which is measured in the rock currently, and water in excess. Therefore, the P – T points during
36 334 retrograde 1, prograde 2 and peak 2 have been interpreted from both of the models. A summary of the
37 335 phase equilibrium models used for each stage of the metamorphic evolution is in Supplementary
38 336 Table 6. The interpreted stages of the P – T path are indicated as grey arrows.
39
40
41
42
43
44
45
46
47
48
49
50
51
52
53
54
55
56
57
58
59
60
61
62
63
64
65

337

5.2.1 Stage 1

The prograde path and peak conditions for the formation of the first mineral assemblage are shown on Figure 8b, after Tamblyn et al. (2019a). Garnet 1 nucleated at the ‘garnet cores in’ line at ~ 0.8–1.1 GPa and approximately 350 °C, based on the core inclusion assemblage of phengite + omphacite + lawsonite + quartz + chlorite + epidote. The path is then interpreted to track up-pressure into the + glaucophane field to satisfy the inclusion relationship of glaucophane in lawsonite and in the core domains of garnet 1 porphyroblasts.

The peak conditions of stage 1 metamorphism are determined from inclusions in the outer part of garnet 1 crystals. We acknowledge that the record of peak 1 has been obliterated by subsequent mineral growth, and as such the interpreted P – T conditions are tentative. We interpret that the lawsonite eclogite reached the phengite + garnet + lawsonite + omphacite + coesite field (based on radial fractures around quartz inclusions), at around 2.9 GPa and 600 °C. This field is bound up-pressure by the conversion of omphacite to jadeite, bound up-temperature by the destabilization of lawsonite, and is bound down-temperature and down-pressure by the loss of coesite or the conversion of coesite to quartz. No inclusions of jadeite were detected, supporting that clinopyroxene remained omphacitic during the metamorphic evolution. Lawsonite is interpreted to have been stable during stage 1 burial as lawsonite preserves ages synchronous with garnet growth (ca. 500 Ma; Tamblyn et al., 2019a), and is ubiquitously found as inclusions in garnet 1. Rare examples of radial fractures around quartz in the outer parts of garnet 1 (Fig. 2e) could indicate the former presence of coesite, further supporting these inferred P – T conditions.

These interpreted peak conditions are supported by the modal proportion of garnet 1. The interface between garnet 1 and 2 is marked by a step increase in X_{Mg} and a prominent increase in X_{Mn} (Fig. 4; 6), together with truncation of core-hosted inclusion trails. The microstructural relationships and change in X_{Mn} and X_{Mg} between the core and the rim strongly imply there was a hiatus in garnet growth. The overall average MnO of the garnet rim is higher than the MnO content of the outer garnet

365 core (Fig. 4), suggesting that there was a period of garnet 1 breakdown prior to the formation of
366 garnet 2. Making the assumption that garnet growth effectively sequesters all available MnO in the
367 rock, particularly at high P - T conditions when chlorite is no longer stable, the higher average MnO
368 concentrations in garnet 2 compared to the outer part of garnet 1 suggests that it originally occupied a
369 larger modal proportion of the rock (Fig. 3a). The original size of the garnets during stage 1 can be
370 calculated using the amount of MnO stored in the MnO dissolution rings in garnet 2. If the outer part
371 of the garnet that formed during stage 1 is assumed to have had a flat MnO profile whose MnO is now
372 incorporated into garnet 2, stage 1 garnet at one point occupied ~ 1.05 times its current modal volume,
373 equivalent to approximately 25 mol% (1-oxide-normalised; Fig. 4a). This is a minimum estimate, as
374 the Mn-rich garnet 2 has been partially broken down and replaced by stage 2 Mn-rich chlorite. The
375 calculated modal proportion of stage 1 garnet porphyroblasts plots at P - T conditions of ~ 2.9 GPa and
376 600 °C (Fig. 8c), within lawsonite stability. The modal proportion of garnet at this stage of the rock's
377 evolution may be overestimated in the phase equilibrium model, by perhaps up to 5 vol % (e.g. Lanari
378 & Engi, 2017), as garnet growth fractionates major elements. This uncertainty in the garnet mode
379 estimate is presented on the phase equilibrium model (Fig. 8b). The calculated modal proportion of
380 garnet passes through the phengite + lawsonite + omphacite + coesite field. The P - T path linking the
381 interpreted prograde assemblages with the peak P - T point passes through talc-bearing P - T space,
382 however the calculated modal proportion of talc is low (< 1 vol%), and as such it is unlikely that talc
383 would have been preserved in the eclogite.

384

385 The retrograde conditions following peak 1 must be interpreted from the phase equilibrium
386 models calculated from the local bulk rock composition, where garnet 1 and lawsonite 1 cores are not
387 part of the chemical system. However, the P - T conditions are difficult to assess, as the water content
388 in the rock at this stage in the lawsonite eclogite's evolution is unknown. Figure 9 shows the phase
389 equilibrium model for the local rock composition with water set to excess (i.e. water saturation), and
390 Figure 10 shows the same composition but with a water content defined by the current mineralogy in
391 the rock. The amount of water currently in the rock is relevant to the assemblages formed during stage
392 2 retrogression, however its relation to the assemblages formed during stage 1 retrogression is

393 unknown. Water content affects the stable mineral assemblages at lower pressures and temperatures,
394 particularly the stability of garnet. The primary mineralogical evidence for stage 1 retrogression is the
395 addition of chlorite + glaucophane to the mineral assemblage (as found as inclusions in garnet and
396 lawsonite rims), and the consumption of garnet 1 rims. As such, the ‘garnet-in’ line is an important
397 indicator of stage 1 retrograde P – T conditions, as it represents the modal volume of garnet in the rock
398 before new stage 2 rims formed. In Figure 9, the garnet-in line occurs in the retrograde assemblage at
399 ~ 1.8–2.1 GPa and 490–500 °C. However, it is unknown if the mineral assemblage was water
400 saturated during retrogression. If the water content was below saturation, we would expect the garnet-
401 in line to move further down pressure and temperature. This can be seen in Figure 10. The difference
402 in position of the garnet-in line is due to water content limiting the formation of chlorite at the
403 expense of garnet. Essentially, this means the garnet-in line in Figure 9 represents the *maximum*
404 pressures and temperatures the rock could have reached during stage 1 retrogression. As water
405 saturation during retrogression seems unlikely, it appears the lawsonite eclogite may have been
406 exhumed to lower pressures and temperatures than can be constrained. In Figure 9, the amount of
407 water in the local bulk composition necessary to destabilize garnet is approximately 6 wt%, 1.35 wt%
408 more than is currently held in hydrous minerals in the rock.

5.3.2 Stage 2

411 Renewed burial leading to the growth of the new garnet rims (garnet 2) is interpreted to start at
412 the ‘garnet rims in’ line (Fig. 9). This is notably only an estimate of the maximum P – T conditions for
413 the start of the prograde path for stage 2, as the water content in the eclogite was unknown as this
414 time, and it may have been exhumed to shallower conditions within the subduction channel but failed
415 to record it. The early stages of the prograde path can be determined using compositions of the cores
416 of stage 2 minerals. Useful compositional parameters are $x(g)$, $z(g)$ and $y(phe)$, where $x(g)$ is the X_{Fe}
417 in garnet, $z(g)$ is the grossular component of garnet, and $y(phe)$ is the proportion of Al on the M2 site
418 in phengite (i.e. dioctahedral Al), a pressure-sensitive parameter. In the P – T model with water in
419 excess, the $x(g)$ and $z(g)$ parameters from the interior of garnet 2 plot at approximately 1.9 GPa and
420 500–510 °C within the prograde field. Notably, the $x(phe)$ and $y(phe)$ parameters from the cores of

421 phengite intersect at approximately 2.2 GPa and 540°C, possibly indicating the initiation of
1
2 422 recrystallisation of phengite at this P – T point. The $x(o)$ parameter from cores of omphacite grains,
3
4 423 which reflects the X_{Fe} , also plots close to these conditions, however as the textural timing of
5
6 424 omphacite growth in this sample is not well known, it is not clear if its compositions reflect stage 1
7
8 425 burial or stage 2 burial. In the P – T model with set water content, these same compositional parameters
9
10 426 plot over a larger range of P – T conditions, however converge towards 1.95 GPa and 450 °C. The
11
12 427 $x(phe)$ and $y(phe)$ parameters from the cores of phengite intersect at the same point as Figure 9: 2.2
13
14 428 GPa and 540°C. As such, an alternative prograde 2 P – T path may have begun at lower pressures and
15
16 429 temperatures and tracked up towards ~ 2.2 GPa and 540 °C.
17
18
19
20 430

21
22 431 The peak assemblage during stage 2 is interpreted to have been phengite + garnet + omphacite +
23
24 432 lawsonite + quartz, which is modelled to occur at conditions of ~ 2.7 GPa and 590 °C. This field
25
26 433 exists identically on both Figure 9 and Figure 10, and is bound up-temperature by the loss of
27
28 434 lawsonite, down-temperature by the presence of talc and/or glaucophane, and up-pressure by the
29
30 435 conversion of quartz to coesite and/or omphacite to jadeite.
31
32

33 436

34
35 437 Stage 2 retrograde P – T conditions are constrained from Figure 10. It is characterised by the
36
37 438 growth of chlorite and retrograde-zoned glaucophane at the expense of garnet and omphacite. It also
38
39 439 includes a modal proportion increase in lawsonite (lawsonite 2), which overgrows garnet 2 (Fig. 2f).
40
41 440 The current modal proportions of all stage 2 minerals – minus the garnet 1 and lawsonite 1 cores
42
43 441 which are not included in the modelling – intersect in the phengite + garnet + lawsonite + omphacite
44
45 442 + quartz + chlorite + glaucophane + H₂O field (Fig. 10c). The modelled isopleths track parallel to
46
47 443 each other down temperature in the H₂O absent field, spanning between 1.8–2.1 GPa (Fig. 10c). Final
48
49 444 recorded retrogression is therefore interpreted to occur down to ~ 2.0 GPa and 520 °C.
50
51
52

53 445

54 446 **5.3 U–Pb titanite geochronology**

55
56 447 In-situ U–Pb isotopic analyses of titanite in the matrix and in the garnet 2 rims define a
57
58 448 common lead trend with a lower intercept of 455.1 ± 9.6 Ma (MSWD = 3.3, $n = 163$, Fig. 11a). The
59
60
61
62
63
64
65

449 upper intercept has a $^{206}\text{Pb}/^{207}\text{Pb}$ ratio of 0.8166 ± 0.0096 . During data processing, 16 analyses were
450 discarded due to low or no signal, and a further 23 analyses were discarded due to contamination from
451 detectable or visible micro-zircons. Incidental ablation of these zircons was visible in the signals as
452 large Zr spikes. U–Pb geochronological data can be found in Supplementary Table 7.

5.4 Ar–Ar phengite geochronology

453
454
455 Step-heating results of two aliquots of phengite from the lawsonite eclogite taken from ~ 50
456 cm apart are shown in Figure 12. The mineral grains come from the rock matrix. Ar–Ar data can be
457 found in Supplementary Table 8. For aliquot 1, an age of 458.4 ± 3.7 Ma was obtained from 72.4% of
458 released ^{39}Ar . Aliquot 2 shows a rise in age with increasing temperature steps. An age of 462.6 ± 3.6
459 Ma was calculated from 61.9% of released ^{39}Ar .

5.5 Rb–Sr phengite geochronology

460
461
462 In-situ LA–ICP–MS Rb–Sr analyses of phengite cores and rims produce almost identical
463 isochrons (Fig. 13). Phengite rims have a wide range of $^{87}\text{Rb}/^{86}\text{Sr}$ ratios and produce an age of $448 \pm$
464 13 Ma (MSWD = 0.61, $n = 18$, Fig. 13a), in many cases with favourably high $^{87}\text{Rb}/^{86}\text{Sr}$ ratios (up to
465 2000). Phengite cores generally have lower $^{87}\text{Rb}/^{86}\text{Sr}$ ratios and produce an age of 437 ± 37 Ma
466 (MSWD = 0.84, $n = 16$, Fig. 13b). When combined, all phengite data give an isochron age of $449 \pm$
467 19 Ma (MSWD = 0.55, $n = 34$, Fig. 13c). Based on textural evidence that titanite occurs as inclusions
468 in phengite, as matrix grains and locally as grains rimming phengite (Fig. 11), it was assumed to have
469 grown synchronously with matrix phengite. Therefore, titanite was analysed to obtain an initial
470 $^{87}\text{Sr}/^{86}\text{Sr}$ ratio to anchor the isochron, producing an average $^{87}\text{Sr}/^{86}\text{Sr}$ ratio of 0.70986 ($n = 6$, Fig. 13d).
471 The rims are interpreted to form during peak metamorphism and thus were used in the final age
472 calculations. When the phengite rims are anchored with the titanite analyses, the isochron age
473 produced is 450 ± 11 Ma (MSWD = 1.09, $n = 26$, Fig. 13e). Rb–Sr geochronological data can be
474 found in Supplementary Table 9.

476

477

5.6 LA-ICP-QQQ isotope mapping

478

Phengite was mapped for ^{85}Rb and ^{87}Sr (Fig. 14). The qualitative results reveal the phengites are zoned, showing enrichments in Sr in the cores of the grains with slight Rb depletion, and Rb enrichments in the rims which correlates to comparatively low levels of Sr. The boundary between these cores and rims is sharp, and in larger grains is aligned along cleavage (Fig. 14). This zoning correlates to zoning seen in the major elements; Sr enriched cores correspond to low Si/high Al cores, and Rb enriched rims correspond to high Si/low Al rims. High Sr grains are titanite. The outline of phengite grains is shown in white.

485

6. DISCUSSION

487

6.1 Petrological evidence for reburial of the lawsonite eclogite

489

Petrographical observations from the block of lawsonite eclogite in the Port Macquarie serpentinite mélangé denote at least two interpretable burial events, summarized in Supplementary Table 1 and schematically outlined in Figure 3.

492

493

Evidence for stage 1 prograde (or burial 1) is preserved in the cores of garnet porphyroblasts, which are prograde-zoned, showing bell-shaped Mn profiles. Lawsonite porphyroblasts grew in equilibrium with garnet, as evidenced by their ca. 500 Ma age, synchronous with garnet growth (Tamblyn et al., 2019a). Stage 1 burial is also recorded by phengite inclusions in the outer part of garnet 1, which are high in Si and low in Al, consistent with crystallization at high pressure. It is possible that rare coesite was formed and captured in the outer parts of garnet 1, interpreted from the presence of radial fractures around quartz.

500

501

The petrologic evidence for a second burial event after partial exhumation is recorded as inclusions within garnet rims, lawsonite rims, and the compositions of matrix minerals. The step increase in X_{Mg} and a Mn oscillation marks the boundary of new garnet 2 growth, and the general

502

503

504

505

504 increased Mn throughout the new garnet rim suggests that it was formed from the breakdown of
1 previously larger garnet porphyroblasts. The presence of chlorite on the boundary between garnet 1
2 505 and garnet 2 is key evidence that lower temperatures and pressures were reached before the growth of
3 506 garnet 2. Omphacite grains in the matrix are prograde zoned (Supp. Fig. 4), and possibly grew from
4 507 the breakdown of glaucophane during the second burial event, however, may also be relic from stage
5 508 1. Phengite and titanite (which make up the strongly foliated rock matrix) underwent recrystallization
6 509 during prograde 2 deformation (e.g. Spencer et al., 2013; de Meyer, 2014; Itaya & Tsujimori, 2015).
7 510 This interpretation is supported by petrological observation that the pervasive foliation in the matrix is
8 511 at an oblique angle to the foliation preserved as inclusion trails in garnet 1 (Fig. 3c). The prograde
9 512 zoning in the phengite is consistent with recrystallization with increasing pressure and temperature,
10 513 however the sharp boundary between zones could either be interpreted as i) progressive prograde
11 514 zoning during total recrystallization of the phengite grains or ii) partial recrystallization of the
12 515 phengite rims at higher pressure, preserving an older low-pressure core. Phengite with low Si/high Al,
13 516 identical to the cores of phengite in the matrix, is preserved in the garnet 2 rims (Fig. 6), providing
14 517 further evidence that garnet 2 rims grew at lower P - T conditions than the outer parts of garnet 1.
15 518 Evidence for stage 2 retrograde includes partial replacement of garnet by chlorite, and partial
16 519 replacement of omphacite by glaucophane and chlorite (Fig. 3d). Retrograde zoning in glaucophane
17 520 (Supp. Fig. 6) supports that it grew during decreasing pressure and temperature. New lawsonite
18 521 growth on existing crystals captured coarse titanite, garnet and glaucophane, suggesting that lawsonite
19 522 increased its modal proportion during retrograde 2 (Fig. 3d).
20 523
21 524

6.2 The origin of oscillatory garnet zoning and the possible role of fluids

525
526
527 Garnets from the lawsonite eclogite show oscillatory zoning in Ca, Mn, Fe and Mg (Fig. 5;
528 Supp. Fig. 2), which is subtle in the outer parts of stage 1 garnet but marked throughout the stage 2
529 garnet rims. Narrow annuli enriched in Mn and Ca are depleted in Fe and Mg, and vice versa. The
530 oscillations are sharp; they occasionally form epitaxial hexagonal crystal shapes on pre-existing
531 garnet (Fig. 5c), or form on irregular-shaped embayed surfaces of pre-existing garnet (Fig. 5b). These

532 features suggest that garnet was resorbed and regrown several times during the metamorphic history
1
2 533 of the lawsonite eclogite (aside from the major garnet resorption event between burial 1 and burial 2).

3
4 534

5
6 535 Garnet resorption and regrowth have been suggested to occur via changes in pressure and
7
8 536 temperature which influence garnet stability (e.g. García-Casco et al., 2002; Kohn, 2004). This
9
10 537 mechanism has been interpreted as the cause of oscillatory garnet zoning from high-pressure rocks in
11
12 538 subduction systems, where seismic instability and/or serpentinite hosted channel circulation cause
13
14 539 cyclic P - T changes (García-Casco et al., 2002; Li et al., 2016, Viete et al., 2018). However, garnet
15
16 540 resorption has also been suggested to be a result of external fluid influx, which dissolves and
17
18 541 reprecipitates garnet in equilibrium with the fluid (Angiboust et al., 2011; Hyppolito et al, 2018).
19
20 542 Additionally, the influx of fluids may enrich or deplete cations incorporated into the garnet during its
21
22 543 growth (e.g. Martin et al., 2011; Angiboust et al., 2014; Park et al., 2017). Such fluid influxes may not
23
24 544 be easy to trace, however the lack of oscillatory zoning in the major elements of other minerals (e.g.
25
26 545 phengite, omphacite) suggests that fluid influxes did not occur on a major scale, or at least were only
27
28 546 recorded in garnet. As there is no petrologic evidence supporting either case, the major element
29
30 547 oscillatory zoning in garnet is interpreted to have formed by subtle fluctuations in P - T and/or influxes
31
32 548 of fluid.
33
34
35
36
37

38 549

40 550 **6.3 P - T conditions of reburial**

41
42 551 The record of the P - T conditions during the first burial event is contained as inclusions in
43
44 552 lawsonite and garnet, while the record of the second burial event is found in garnet and lawsonite rims
45
46 553 and the matrix mineralogy. The P - T path proposed is summarised in Figure 15, the interpreted
47
48 554 conditions are summarised in Supplementary Table 6. The proposed P - T path is tentative, due to the
49
50 555 difficulty in reconstructing the mineralogical evolution of the sample.
51
52

53 556

54
55 557 The P - T path during stage 1 burial is recorded from 0.8–1.1 GPa at approximately 350 °C,
56
57 558 and then tracks up to peak conditions of at least 2.9 GPa and 600 °C based on lawsonite stability,
58
59 559 inclusion assemblages in lawsonite and garnet and the estimated modal proportion of garnet (Fig. 8).
60
61
62
63
64
65

1 560 The potential former presence of coesite, now recorded by radial fractures around quartz inclusions in
2 561 the outer parts of garnet 1, supports these peak conditions. High Si/low Al phengite inclusions in the
3
4 562 outer parts of garnet 1 also support that high-pressures were reached during this stage (Fig. 6).
5
6 563 Subsequent retrogression to maximum conditions of ~ 2.0 GPa and 500 °C is recorded by the
7
8 564 consumption of garnet, and growth of chlorite and glaucophane (Fig. 9; 10). It is likely the lawsonite
9
10 565 eclogite reached lower pressures and temperatures than this during retrogression, however this part of
11
12 566 its evolution is difficult to reconstruct.
13
14

15 567

17 568 Stage 2 reburial began at maximum conditions of ~ 2.0 GPa and 500 °C. Growth of new
18
19 569 garnet rims with elevated Mn and X_{Mg} captured the stage 1 chlorite and glaucophane. Stage 2 peak
20
21 570 conditions of 2.7 GPa and 590 °C were reached, based on the preserved peak mineral assemblage.
22
23 571 Retrogression to approximately 1.9 GPa and 520 °C is based on the current modal mineralogy of the
24
25 572 rock (Fig. 10c), and is supported by the formation of retrograde-zoned glaucophane and the partial
26
27 573 break down of garnet to form chlorite.
28
29

30 574

32 575 If these tentative estimates are taken at face value, the earliest stages of the prograde
33
34 576 evolution of the rock occurred on a geothermal gradient of approximately 370 °C/GPa, while the peak
35
36 577 and retrograde stages of both stage 1 and 2 occurred on a cooler geothermal gradient of approximately
37
38 578 210–265 °C/GPa. These gradients are in line with a subduction channel which is cooling over time,
39
40 579 potentially in response to the refrigeration effects of on-going subduction (Gerya, 2002; Agard et al.,
41
42 580 2018). If this is correct, it suggests the eclogite records the transition from subduction initiation (e.g.
43
44 581 Tamblyn et al., 2019a) to subduction maturity. These inferred geothermal estimates are comparable to
45
46 582 the geothermal gradient experienced by garnet blueschist from the same mélange that hosts the
47
48 583 lawsonite eclogite at Port Macquarie (~ 275 °C/GPa; Tamblyn et al., 2019a). The complete P – T path
49
50 584 suggested in Figure 15 is two hair-pin loops, which are constrained by the presence of lawsonite
51
52 585 throughout the recorded history. Such P – T evolutions have been previously suggested for high-
53
54 586 pressure rocks in oceanic subduction systems (e.g. Gerya et al, 2002; Krebs et al., 2011; Pourteau et
55
56 587 al., 2019).
57
58
59
60
61
62
63
64
65

588

589

6.4 Timing of reburial

590

Tamblyn et al. (2019a) obtained Lu–Hf ages of 489.7 ± 5 Ma for garnet–whole rock and 505 ± 15 Ma for lawsonite–whole rock from the eclogite. The cores of stage 1 garnet are highly enriched in Lu compared to the stage 2 garnet, indicating the garnet Lu–Hf age is essentially the age of stage 1 garnet growth. The lawsonite Lu–Hf age is less precise but within uncertainty of the garnet age, suggesting that stage 1 garnet and stage 1 lawsonite grew within a single isotopic reservoir at ca. 500–490 Ma. The lawsonite grains contain patches that are enriched in Lu (Tamblyn et al., 2019a), and in places are overgrown by volumetrically minor second generation lawsonite (Fig. 2f). The Lu-rich domains in stage 1 lawsonite formed prior to garnet nucleation. The P – T path during the stage 1 burial tracks up to tentative peak conditions of at least 2.9 GPa and 600 °C (section 6.3). This occurred at ca. 505–490 Ma as dated by garnet and lawsonite Lu–Hf (Tamblyn et al., 2019a; Fig. 15).

600

601

Matrix phengite that encloses garnet, lawsonite and omphacite porphyroblasts shows an increasing Si and celadonite content from core to rim (Fig. 6; Carswell et al., 2000). This compositional component is consistent with increasing pressure, which in the absence of information about changes in non-lithostatic stress, equates to increasing burial depth. The plateau ages obtained from Ar–Ar geochronology from phengite from the rock matrix give ages of ca. 458 and ca. 462 Ma. The suggested closure temperature of argon diffusion in phengite is variable (e.g. Warren et al., 2011; Fornash et al., 2016), and is dependent on grain size and fluid availability (e.g. Glodny et al., 2002). Numerical diffusion modelling suggests that phengite grown at blueschist to eclogite facies (up to 550 °C) can retain argon from its prograde history (Warren et al., 2011). This has been supported by step-heating experiments which suggest phengite can be highly retentive of argon (Forster and Lister, 2014). These findings are in line with samples from high-pressure terranes where Ar–Ar ages are similar to peak metamorphic ages obtained from zircon or garnet geochronology (Fornash et al., 2016), or can be texturally related to mineral growth during sequential phases of deformation (Putlitz et al., 2005).

615

616 In-situ LA-ICP-MS Rb-Sr dating of mica is still in its infancy as a geochronological
1
2 617 technique. However, it has the potential to rapidly constrain ages of metamorphism and deformation
3
4 618 in metamorphic rocks. Rb-Sr analyses of phengite rims, coupled with an initial $^{87}\text{Sr}/^{86}\text{Sr}$ value from
5
6 619 texturally intergrown titanite, give an isochron age of ca. 450 Ma. The rims of phengite were selected
7
8 620 for the final age calculation, as they are interpreted to grow at peak conditions of stage 2.

10
11 621

12
13 622 Rb and Sr maps also support that the geochronologic results are growth ages (Fig. 14); the
14
15 623 zoning is sharply defined, suggesting minimal post-growth diffusion within the grains (e.g. Konrad-
16
17 624 Schmolke et al., 2011). Rb-Sr maps show Sr enrichments in the low-Si cores of phengite, and Rb
18
19 625 enrichments in the high-Si rims, a pattern that has been noted in high-pressure rocks (Di Vincenzo et
20
21 626 al., 2006). The incorporation of Sr into phengite may therefore be related to the breakdown of another
22
23 627 Sr-bearing mineral in the system at lower pressures, or, a preference for Sr in low-Si less-phengitic
24
25 628 white mica, which declines with increasing phengitic component up-pressure. The Rb-Sr age of the
26
27 629 phengite rims is within uncertainty of the age obtained from phengite Ar-Ar analyses and titanite U-
28
29 630 Pb age of ca. 455 Ma (below). This interpretation is in line with similar high-pressure terranes, where
30
31 631 Rb-Sr dates record crystallization of phengite on the prograde-peak path during metamorphism (e.g.
32
33 632 Hetzel & Romer, 2000; Glodny et al., 2002; Bosse et al., 2005; Di Vincenzo et al., 2006). In some of
34
35 633 these examples, Rb-Sr phengite growth ages are synchronous with Ar-Ar phengite ages
36
37 634 (Anczkiewicz et al., 2000; Hetzel & Romer, 2000; Glodny et al., 2002; Rodríguez et al., 2003). Rb-Sr
38
39 635 has also been shown to date continuous recrystallization of white mica during retrograde deformation
40
41 636 in polymetamorphic terranes, at peak temperatures of ~ 500–550 °C (Bröcker et al., 2013),
42
43 637 demonstrating the ability for the Rb-Sr white mica ages to record recrystallization events.
44
45
46
47
48

49 638

50
51 639 The U-Pb data from titanite in the matrix and as inclusions in the stage 2 garnet gives an age
52
53 640 of ca. 455 Ma. Although there is some dispersion in the data, it is evident the matrix titanites are
54
55 641 significantly younger than the ca. 490 Ma age for stage 1 lawsonite and garnet. Phase equilibrium
56
57 642 modelling suggests the rock experienced P - T conditions below the closure temperature of titanite
58
59 643 (~600–800 °C; Hartnady et al., 2019). Additionally, there is no evidence of a rutile-bearing
60
61
62
63
64
65

644 assemblage in the lawsonite eclogite. Therefore, it is unlikely the titanite formed from breakdown of
1
2 645 rutile on the retrograde path. Consequently, we interpret the titanite U–Pb data to reflect the timing of
3
4 646 titanite recrystallisation.
5

6
7 647
8
9 648 Titanite occurs throughout the matrix and forms around the edges of prograde-zoned phengite
10
11 649 (Fig. 11b-d). It occurs as fine-grained inclusion trails in garnet cores and lawsonite, and as coarse-
12
13 650 grained inclusions in stage 2 garnet and lawsonite rims (Fig. 11b-c). These textural relationships
14
15 651 indicate that titanite was stable during the entire metamorphic evolution of the eclogite, first growing
16
17 652 during the stage 1 burial event, and recrystallizing during the prograde evolution of the stage 2 burial
18
19 653 event to form coarser-grained titanite. This recrystallization was possibly tracked by increasing F,
20
21 654 Al₂O₃ and FeO content in the titanite (Fig. 7).
22
23

24 655
25
26 656 The inclusions in titanite are limited to fine-grained apatite, phengite and zircon (< 10 µm).
27
28 657 Zircon is either euhedral and 5–10 µm in size, or occurs as fine-grained clusters or web-like
29
30 658 intergrowths which are 2 µm or less (Fig. 11b,c). The 5–10 µm sized apatite, phengite and zircon
31
32 659 inclusions are interpreted to predate the crystallization of titanite, and were avoided during analyses.
33
34 660 However, the extremely fine-grained web-like micro-zircon was difficult to avoid, and was possibly
35
36 661 incorporated into analyses. This is suggested by Zr concentrations in the titanite analyses of up to ~
37
38 662 18800 ppm (Supp. Table 7). Texturally, these extremely fine-grained zircon dustings only occur in
39
40 663 sections of titanite grains, and are absent in phengite, garnet, lawsonite and omphacite. This suggests
41
42 664 they are probably exsolution of Zr from the titanite, rather than inclusions (Fig. 11b,c). Titanite can
43
44 665 substitute Zr⁴⁺ for Ti⁴⁺ in its crystal lattice, as evidenced by development of the Zr-in-titanite
45
46 666 thermobarometer (Hayden et al., 2008). However, in quartz-absent rocks, titanite can take in
47
48 667 significant amounts of ZrO₂ (up to 15 wt%; Della Ventura et al., 1999; Seifert & Kramer, 2003;
49
50 668 Seifert, 2005; Vuorinen & Hålenius, 2005; Liferovich & Mitchell, 2005; Chakhmouradian, 2004).
51
52 669 While these studies are from igneous rocks, they demonstrate the ability for significant Zr to
53
54 670 substitute into titanite.
55
56 671
57
58
59
60
61
62
63
64
65

1
2
3
4
5
6
7
8
9
10
11
12
13
14
15
16
17
18
19
20
21
22
23
24
25
26
27
28
29
30
31
32
33
34
35
36
37
38
39
40
41
42
43
44
45
46
47
48
49
50
51
52
53
54
55
56
57
58
59
60
61
62
63
64
65

672 The phase equilibrium modelling of the stage 2 effective bulk composition suggests the
673 prograde-peak path taken by the lawsonite eclogite during reburial was quartz-free until absolute peak
674 conditions were obtained (590 °C, 2.7 GPa). Zircon exsolution from titanite has not been directly
675 reported before, but in lieu of other explanations, we suggest these fine-grained clusters of zircon
676 within titanite represent high-Zr titanite which formed in a quartz absent matrix assemblage, which
677 then exsolved zircon after crystallization of the parent mineral. As such, while we tried to avoid areas
678 of obvious weblike zircon in titanite, we suggest that if small amounts of fine-grained zircon
679 exsolution were incorporated into the titanite U–Pb analyses, we are dating U–Pb isotopic ratios
680 related to titanite recrystallization at ca. 455 Ma.

681
682 The above interpretations suggest recrystallization of phengite and titanite at ca. 450 Ma dates
683 the timing of burial 2, which reached peak P – T conditions of 2.7 GPa and 590 °C. The two burial
684 events were separated by a period of exhumation to maximum conditions of approximately 2.0 GPa
685 and 500 °C, however the lawsonite eclogite may have been exhumed further up the subduction
686 channel. The two stages of metamorphism and burial in the lawsonite eclogite occurred over a period
687 of at least ca. 50 M.y. (Fig. 15). The timing of final exhumation after burial 2 is unknown, but had
688 occurred by the Permian, based on serpentinite detritus in nearby early Permian basins in the SNEO
689 (Aitchison et al., 1994).

690 691 **6.5 Examples of other burial cycles**

692 The suggestion that the block of lawsonite eclogite at Port Macquarie underwent two stages
693 of burial, each marked by garnet growth and separated by a stage of garnet breakdown, is similar to
694 P – T histories proposed from other studies on subducted rocks in oceanic settings, and is supported by
695 results of numerical modelling (e.g. Gerya et al., 2002). Despite the difficulties in recognizing and
696 constraining multiple cycles of burial and exhumation within single high-pressure samples, workers
697 have had success using various geochronological and mineralogical tools. Dating zones within
698 metamorphic zircon, combined with REE chemistry and inclusion assemblages, have allowed two or
699 more subduction cycles to be identified in Rhodope, Greece (Liati et al., 2016) and the Italian Alps

1
2 701 (Rubatto et al., 2011), however the latter was within a continental subduction system. Three burial
3
4 702 cycles in the Sambagawa belt in Japan have been identified from mineral assemblages and mineral
5
6 703 chemistry of garnet and amphibole in eclogite by Kabir & Takasu (2010). Two burial cycles are
7
8 704 recorded in eclogite from the Akeyazi terrane in Tianshan, China, interpreted from petrological and
9
10 705 mineral zoning evidence, with P - T paths constrained from pseudosections (Li et al., 2016). García-
11
12 706 Casco et al. (2002) modelled oscillatory zoning in garnet and amphibole chemistry from serpentinite
13
14 707 mélangé in Cuba, concluding that they formed in near-equilibrium and record fluctuations in P - T
15
16 708 conditions during subduction. Blanco-Quintero et al. (2011) also reported reburial during interpreted
17
18 709 large-scale convective flow from this mélangé, interpreted from garnet zoning and P - T pseudosection
19
20 710 modelling. Geochronological constraints on the development of the mineral assemblages in the Port
21
22 711 Macquarie eclogite point to a long history of high-pressure metamorphism, with a significant age
23
24 711 difference between the formation of stage 1 and stage 2 assemblages (Fig. 15). Based on time scales
25
26 712 of material movement in subduction systems from numerical modelling (Gerya et al., 2002), the
27
28 713 geochronological data from the eclogite supports the likelihood that multiple burial and partial
29
30 714 exhumation paths may have occurred.

31
32
33 715

34 35 716 **6.6 Subduction channel dynamics**

36
37 717

38
39
40 718 A corner or return flow model of material within the subduction channel (e.g. Shreve & Cloos,
41
42 719 1986, Gerya et al., 2002; Agard et al., 2009; Roda et al., 2019), is suggested for repeated burial and
43
44 720 exhumation of the lawsonite eclogite at Port Macquarie. Numerical modelling predicts that during
45
46 721 oceanic subduction, hydration of the mantle wedge creates a buoyant low viscosity serpentinite-filled
47
48 722 subduction channel which can pluck high-pressure rocks from the subducting slab and circulate them
49
50 723 within the channel (e.g. Gerya et al., 2002). In these models, the high-pressure fragments can become
51
52 724 deeply subducted, but can also experience partial exhumation and reburial, resulting in P - T loops
53
54 725 (Gerya et al., 2002). Rocks with different P - T - t histories can also accumulate within the channel and
55
56 726 be exhumed together to form mélanges that contain a variety of subducted products (e.g. Krebs et al.,
57
58 727 2008). At Port Macquarie, this behaviour is confirmed by the presence of garnet blueschist, which is
59
60
61
62
63
64
65

1
2 729 ca. 470 Ma in age, and has a different P - T path to the eclogite, yet is found as a tectonic block less
3 than 10 meters away from the lawsonite eclogite (Och et al., 2003; Tamblyn et al., 2019a).

4 730

5
6 731 The geochronological data presented above also supports the notion of long-lived residence of
7 high-pressure materials within oceanic subduction channels. The minimum duration spent in the
8
9 732 subduction channel by the lawsonite eclogite at Port Macquarie is ca. 50 M.y. (Fig. 15). Analogous
10 733 durations of high-pressure metamorphism and accumulation have been reported from oceanic
11 734 subduction systems. Exotic high-pressure rocks hosted in serpentinite, which have been interpreted to
12 735 have been buried and exhumed by convective flow processes, span an age range of ca. 55 M.y. in
13 736 Cuba (Lázaro et al., 2009), and ca. 40 M.y. in the Dominican Republic (Krebs et al., 2008). High-
14 737 pressure rocks exhumed in Turkey with different P - T - t histories span an age range of ca. 20 M.y.
15 738 (Pourteau et al., 2019), supported by in-situ Ar-Ar data (Fornash et al., 2016). In the Mariana
16 739 subduction system, the residence time for blueschist within the subduction channel is ca. 48 M.y.
17 740 (Tamblyn et al., 2019b).

18 741

19 742
20 743 With the caveat that the P - T conditions suggested from the phase equilibrium modelling of
21 744 the eclogite at Port Macquarie are taken as approximations, a P - T - t path can be constructed for the
22 745 lawsonite eclogite, and the rate of exhumation to reburial estimated. If the maximum possible P - T
23 746 conditions of stage 1 exhumation are taken as 2.0 GPa and 500 °C, the total pressure and temperature
24 747 change from peak stage 1 to peak stage 2 equates to ~ 1.6 GPa and 190 °C. If an average lithostatic
25 748 pressure of 3.2 km/kbar with no non-lithostatic loads is assumed, this pressure change is equivalent to
26 749 approximately 50 km of vertical depth change. Depending on subduction angle, the total travel
27 750 distance of the lawsonite eclogite within the channel may have been more than 100 km during the
28 751 looping P - T history.

29 752

30 753

31 754 7. CONCLUSIONS

32 755

1
2 757 Lawsonite eclogite in serpentinite mélangé at Port Macquarie in the Southern New England
3
4 758 Orogen records P – T conditions of ~ 2.9 GPa and 600 °C, attained at ca. 500 – 490 Ma. The mineral
5
6 759 assemblages that define these P – T conditions were overprinted by a second high-pressure
7
8 760 assemblage that formed at ca. 450 Ma. Compositional zoning in phengite, and growth of a second
9
10 761 generation of garnet, indicate the overprinting mineral assemblage formed during up-pressure
11
12 762 metamorphism to ~ 2.7 GPa and 590 °C. Between these two stages of burial, partial exhumation
13
14 763 occurred to at least 2.0 GPa, but probably to lower P – T conditions. The P – T evolution defines hair-
15
16 764 pin looping P – T paths that developed along a similar geothermal gradient, suggesting the lawsonite
17
18 765 eclogite was cycled within a serpentinite-filled subduction channel during return flow of subducted
19
20 766 material. This cycling occurred over a minimum timeframe of ca 50 M.y., implying long-lived
21
22 767 residence of the eclogite within the subduction system. A number of studies are beginning to
23
24 768 discover that subducted material may undergo complex P – T – t evolutions that record multiple
25
26 769 episodes of burial and exhumation during prolonged residence within subduction systems. These
27
28 770 cyclic P – T evolutions support predictions from numerical models which suggest material can follow
29
30 771 convective flow paths within evolving serpentinite filled subduction channels.

31
32
33 771

34
35 772 *Acknowledgements*

36
37
38 773 The authors would like to thank Ben Wade and Sarah Gilbert of Adelaide Microscopy, for their
39
40 774 assistance with EPMA and LA–ICP–MS data collection. David Kelsey is thanked for helpful
41
42 775 discussions and his ongoing support with phase equilibria modelling. Jack Gillespie of Curtin
43
44 776 University is thanked for collecting the phase and EDS maps. Mitchell Bockmann of the University
45
46 777 of Adelaide is thanked for setting up the titanite U–Pb method. We thank Pierre Lanari and an
47
48 778 anonymous reviewer for their comments, which greatly strengthened the manuscript. This research
49
50 779 in part was supported by Australian Research Council grant DP160104637. Renée Tamblyn
51
52 780 acknowledges support from the University of Adelaide in the form of the Aldermann Kleeman
53
54 781 travel scholarship and an Australian Postgraduate Award.

55
56
57 782

58
59 783 *References*

60
61
62
63
64
65

784

1
2 785 Agard, P., Plunder, A., Angiboust, S., Bonnet, G., & Ruh, J. (2018). The subduction plate interface:

3
4 786 Rock record and mechanical coupling (from long to short time scales). *Lithos*.

5
6 787 Agard, P., Yamato, P., Jolivet, L., & Burov, E. (2009). Exhumation of oceanic blueschists and

7
8 788 eclogites in subduction zones: timing and mechanisms. *Earth-Science Reviews*, 92(1), 53-79.

9
10 789 Aitchison, J. C., Blake, M. C., Flood, P. G., & Jayko, A. S. (1994). Paleozoic ophiolitic assemblages

11
12 790 within the southern New England orogen of eastern Australia: Implications for growth of the

13
14 791 Gondwana margin. *Tectonics*, 13(5), 1135-1149. doi: 10.1029/93TC03550

15
16 792 Anczkiewicz, R., Burg, J., Villa, I. M., & Meier, M. (2000). Late Cretaceous blueschist

17
18 793 metamorphism in the Indus suture zone, Shangla region, Pakistan Himalaya. *Tectonophysics*,

19
20 794 324(1-2), 111-134.

21
22 795 Anczkiewicz, R., Platt, J. P., Thirlwall, M. F., & Wakabayashi, J. (2004). Franciscan subduction off to

23
24 796 a slow start: evidence from high-precision Lu–Hf garnet ages on high grade-blocks. *Earth*

25
26 797 and Planetary Science Letters, 225(1), 147-161.

27
28 798 Anczkiewicz, R., Szczepański, J., Mazur, S., Storey, C., Crowley, Q., Villa, I. M., Thirlwall, M. F., &

29
30 799 Jeffries, T. E. (2007). Lu–Hf geochronology and trace element distribution in garnet:

31
32 800 implications for uplift and exhumation of ultra-high pressure granulites in the Sudetes, SW

33
34 801 Poland. *Lithos*, 95(3-4), 363-380.

35
36 802 Angiboust, S., Agard, P., Raimbourg, H., Yamato, P., & Huet, B. (2011). Subduction interface

37
38 803 processes recorded by eclogite-facies shear zones (Monviso, W. Alps). *Lithos*, 127(1-2), 222-

39
40 804 238.

41
42 805 Angiboust, S., Pettke, T., De Hoog, J. C., Caron, B., & Oncken, O. (2014). Channelized fluid flow

43
44 806 and eclogite-facies metasomatism along the subduction shear zone. *Journal of Petrology*,

45
46 807 55(5), 883-916.

47
48 808 Baitsch-Ghirardello, B., Gerya, T. V., & Burg, J.-P. (2014). Geodynamic regimes of intra-oceanic

49
50 809 subduction: Implications for arc extension vs. shortening processes. *Gondwana Research*,

51
52 810 25(2), 546-560.

53
54
55
56
57
58
59
60
61
62
63
64
65

- 1
2
3
4
5
6
7
8
9
10
11
12
13
14
15
16
17
18
19
20
21
22
23
24
25
26
27
28
29
30
31
32
33
34
35
36
37
38
39
40
41
42
43
44
45
46
47
48
49
50
51
52
53
54
55
56
57
58
59
60
61
62
63
64
65
- 811 Blanco-Quintero, I. F., García-Casco, A., & Gerya, T. V. (2011). Tectonic blocks in serpentinite
812 mélange (eastern Cuba) reveal large-scale convective flow of the subduction channel.
813 *Geology*, 39(1), 79-82.
- 814 Bosse, V., Féraud, G., Balleve, M., Peucat, J.-J., & Corsini, M. (2005). Rb–Sr and ⁴⁰Ar/³⁹Ar ages in
815 blueschists from the Ile de Groix (Armorican Massif, France): implications for closure
816 mechanisms in isotopic systems. *Chemical Geology*, 220(1-2), 21-45.
- 817 Bröcker, M., Baldwin, S., & Arkudas, R. (2013). The geological significance of ⁴⁰Ar/³⁹Ar and Rb–
818 Sr white mica ages from S yros and S ifnos, G reece: a record of continuous (re)
819 crystallization during exhumation? *Journal of metamorphic Geology*, 31(6), 629-646.
- 820 Carswell, D., Wilson, R., & Zhai, M.-g. (2000). Metamorphic evolution, mineral chemistry and
821 thermobarometry of schists and orthogneisses hosting ultra-high pressure eclogites in the
822 Dabieshan of central China. *Lithos*, 52(1-4), 121-155.
- 823 Castelli, D., & Rubatto, D. (2002). Stability of Al- and F-rich titanite in metacarbonate: petrologic and
824 isotopic constraints from a polymetamorphic eclogitic marble of the internal Sesia Zone
825 (Western Alps). *Contributions to Mineralogy and Petrology*, 142(6), 627-639.
- 826 Chakhmouradian, A. R. (2004). Crystal chemistry and paragenesis of compositionally unique (Al-,
827 Fe-, Nb-, and Zr-rich) titanite from Afrikanda, Russia. *American Mineralogist*, 89(11-12),
828 1752-1762.
- 829 Cherniak, D. (2006). Zr diffusion in titanite. *Contributions to Mineralogy and Petrology*, 152(5), 639-
830 647.
- 831 Collins, W., & Richards, S. (2008). Geodynamic significance of S-type granites in circum-Pacific
832 orogens. *Geology*, 36(7), 559-562.
- 833 Collins, W. J. (2002). Nature of extensional accretionary orogens. *Tectonics*, 21(4).
- 834 de Meyer, C. M., Baumgartner, L. P., Beard, B. L., & Johnson, C. M. (2014). Rb–Sr ages from
835 phengite inclusions in garnets from high pressure rocks of the Swiss Western Alps. *Earth and*
836 *Planetary Science Letters*, 395, 205-216.
- 837 Della Ventura, G., Bellatreccia, F., & Williams, C. (1999). Zr- and LREE-rich titanite from Tre Croci,
838 Vico volcanic complex (Latium, Italy). *Mineralogical Magazine*, 63(1), 123-130.

- 839 Di Vincenzo, G., Tonarini, S., Lombardo, B., Castelli, D., & Ottolini, L. (2006). Comparison of
1
2 840 ^{40}Ar – ^{39}Ar and Rb – Sr data on phengites from the UHP Brossasco–Isasca Unit (Dora Maira
3
4 841 Massif, Italy): implications for dating white mica. *Journal of Petrology*, 47(7), 1439-1465.
5
6 842 Diener, J., & Powell, R. (2012). Revised activity–composition models for clinopyroxene and
7
8 843 amphibole. *Journal of metamorphic Geology*, 30(2), 131-142.
9
10 844 Dodson, M. H. (1973). Closure temperature in cooling geochronological and petrological systems.
11
12 845 *Contributions to Mineralogy and Petrology*, 40(3), 259-274.
13
14 846 Elburg, M., Bons, P., Foden, J., & Brugger, J. (2003). A newly defined Late Ordovician magmatic-
15
16 847 thermal event in the Mt Painter Province, northern Flinders Ranges, South Australia.
17
18 848 *Australian Journal of Earth Sciences*, 50(4), 611-631.
19
20 849 Elburg, M., Vroon, P., van der Wagt, B., & Tchalikian, A. (2005). Sr and Pb isotopic composition of
21
22 850 five USGS glasses (BHVO-2G, BIR-1G, BCR-2G, TB-1G, NKT-1G). *Chemical Geology*,
23
24 851 223(4), 196-207.
25
26 852 Evans, T. (2004). A method for calculating effective bulk composition modification due to crystal
27
28 853 fractionation in garnet- bearing schist: implications for isopleth thermobarometry. *Journal of*
29
30 854 *metamorphic Geology*, 22(6), 547-557.
31
32 855 Fornash, K. F., Cosca, M. A., & Whitney, D. L. (2016). Tracking the timing of subduction and
33
34 856 exhumation using $^{40}\text{Ar}/^{39}\text{Ar}$ phengite ages in blueschist-and eclogite-facies rocks
35
36 857 (Sivrihisar, Turkey). *Contributions to Mineralogy and Petrology*, 171(7), 67.
37
38 858 Forster, M. A., & Lister, G. S. (2014). $^{40}\text{Ar}/^{39}\text{Ar}$ geochronology and the diffusion of ^{39}Ar in
39
40 859 phengite–muscovite intergrowths during step-heating experiments in vacuo. *Geological*
41
42 860 *Society, London, Special Publications*, 378(1), 117-135.
43
44 861 Fukui, S., Watanabe, T., Itaya, T., & Leitch, E. C. (1995). Middle Ordovician high PT metamorphic
45
46 862 rocks in eastern Australia: Evidence from K- Ar ages. *Tectonics*, 14(4), 1014-1020.
47
48 863 Gaidies, F., De Capitani, C., & Abart, R. (2008). THERIA_G: a software program to numerically
49
50 864 model prograde garnet growth. *Contributions to Mineralogy and Petrology*, 155(5), 657-671.
51
52
53
54
55
56
57
58
59
60
61
62
63
64
65

- 865 García- Casco, A., Torres- Roldán, R., Millán, G., Monié, P., & Schneider, J. (2002). Oscillatory
1 zoning in eclogitic garnet and amphibole, Northern Serpentinite Melange, Cuba: a record of
2
3
4 867 tectonic instability during subduction? *Journal of metamorphic Geology*, 20(6), 581-598.
5
6 868 Gerya, T. V., Stöckhert, B., & Perchuk, A. L. (2002). Exhumation of high- pressure metamorphic
7
8
9 869 rocks in a subduction channel: A numerical simulation. *Tectonics*, 21(6).
10
11 870 Glen, R. (2013). Refining accretionary orogen models for the Tasmanides of eastern Australia.
12
13 871 *Australian Journal of Earth Sciences*, 60(3), 315-370.
14
15 872 Glodny, J., Bingen, B., Austrheim, H., Molina, J. F., & Rusin, A. (2002). Precise eclogitization ages
16
17 873 deduced from Rb/Sr mineral systematics: the Maksyutov complex, Southern Urals, Russia.
18
19 874 *Geochimica et Cosmochimica Acta*, 66(7), 1221-1235.
20
21 875 Green, E., Holland, T., & Powell, R. (2007). An order-disorder model for omphacitic pyroxenes in the
22
23 876 system jadeite-diopsidehedenbergite-acmite, with applications to eclogitic rocks. *American*
24
25 877 *Mineralogist*, 92(7), 1181-1189.
26
27 878 Hartnady, M. I., Kirkland, C. L., Clark, C., Spaggiari, C. V., Smithies, R. H., Evans, N. J., &
28
29 879 McDonald, B. J. (2019). Titanite dates crystallization: Slow Pb diffusion during super-
30
31 880 solidus re- equilibration. *Journal of metamorphic Geology*, 37(6), 823-838.
32
33 881 Hayden, L. A., Watson, E. B., & Wark, D. A. (2008). A thermobarometer for sphene (titanite).
34
35 882 *Contributions to Mineralogy and Petrology*, 155(4), 529-540.
36
37 883 Hetzel, R., & Romer, R. L. (2000). A moderate exhumation rate for the high- pressure Maksyutov
38
39 884 Complex, southern Urals, Russia. *Geological Journal*, 35(3- 4), 327-344.
40
41 885 Hogmalm, K. J., Zack, T., Karlsson, A. K.-O., Sjöqvist, A. S., & Garbe-Schönberg, D. (2017). In situ
42
43 886 Rb–Sr and K–Ca dating by LA-ICP-MS/MS: an evaluation of N₂O and SF₆ as reaction
44
45 887 gases. *Journal of Analytical Atomic Spectrometry*, 32(2), 305-313.
46
47
48
49 888 Holland, T., & Powell, R. (1998). An internally consistent thermodynamic data set for phases of
50
51 889 petrological interest. *Journal of metamorphic Geology*, 16(3), 309-343.
52
53 890 Holland, T., & Powell, R. (2003). Activity–composition relations for phases in petrological
54
55 891 calculations: an asymmetric multicomponent formulation. *Contributions to Mineralogy and*
56
57 892 *Petrology*, 145(4), 492-501.
58
59
60
61
62
63
64
65

- 893 Holland, T., & Powell, R. (2011). An improved and extended internally consistent thermodynamic
1 dataset for phases of petrological interest, involving a new equation of state for solids.
2
3
4 895 *Journal of metamorphic Geology*, 29(3), 333-383.
5
- 6 896 Itaya, T., & Tsujimori, T. (2015). White mica K–Ar geochronology of Sanbagawa eclogites from
7
8 897 Southwest Japan: implications for deformation-controlled K–Ar closure temperature.
9
10 898 *International Geology Review*, 57(5-8), 1014-1022.
11
- 12 899 Jenkins, R., Landenberger, B., & Collins, W. (2002). Late Palaeozoic retreating and advancing
13
14 900 subduction boundary in the New England fold belt, New South Wales. *Australian Journal of*
15
16 901 *Earth Sciences*, 49(3), 467-489.
17
- 18 902 Jessop, K., Daczko, N., & Piazzolo, S. (2019). Tectonic cycles of the New England Orogen, eastern
19
20 903 Australia: A review. *Australian Journal of Earth Sciences*, 66(4), 459-496.
21
22
- 23 904 Kabir, M., & Takasu, A. (2010). Evidence for multiple burial–partial exhumation cycles from the
24
25 905 Onodani eclogites in the Sambagawa metamorphic belt, central Shikoku, Japan. *Journal of*
26
27 906 *metamorphic Geology*, 28(8), 873-893.
28
- 29 907 Kelley, S. (2002). Excess argon in K–Ar and Ar–Ar geochronology. *Chemical Geology*, 188(1), 1-22.
30
31
- 32 908 Kemp, A., Hawkesworth, C., Collins, W., Gray, C., & Blevin, P. (2009). Isotopic evidence for rapid
33
34 909 continental growth in an extensional accretionary orogen: The Tasmanides, eastern Australia.
35
36 910 *Earth and Planetary Science Letters*, 284(3), 455-466.
37
- 38 911 Kohn, M. J. (2004). Oscillatory- and sector- zoned garnets record cyclic (?) rapid thrusting in central
39
40 912 Nepal. *Geochemistry, Geophysics, Geosystems*, 5(12).
41
- 42 913 Konrad-Schmolke, M., O'Brien, P. J., de Capitani, C., & Carswell, D. A. (2008). Garnet growth at
43
44 914 high-and ultra-high pressure conditions and the effect of element fractionation on mineral
45
46 915 modes and composition. *Lithos*, 103(3-4), 309-332.
47
- 48 916 Krebs, M., Maresch, W., Schertl, H.-P., Münker, C., Baumann, A., Draper, G., Idleman, B., & Trapp,
49
50 917 E. (2008). The dynamics of intra-oceanic subduction zones: a direct comparison between
51
52 918 fossil petrological evidence (Rio San Juan Complex, Dominican Republic) and numerical
53
54 919 simulation. *Lithos*, 103(1), 106-137.
55
56
57
58
59
60
61
62
63
64
65

- 920 Krebs, M., Schertl, H.-P., Maresch, W., & Draper, G. (2011). Mass flow in serpentinite-hosted
1 subduction channels: P–T–t path patterns of metamorphic blocks in the Rio San Juan mélange
2
3
4 922 (Dominican Republic). *Journal of Asian Earth Sciences*, 42(4), 569-595.
5
- 6 923 Lanari, P., & Engi, M. (2017). Local bulk composition effects on metamorphic mineral assemblages.
7
8 924 *Reviews in mineralogy and geochemistry*, 83(1), 55-102.
9
- 10 925 Lázaro, C., García- Casco, A., Rojas Agramonte, Y., Kröner, A., Neubauer, F., & Iturralde- Vinent,
11
12 926 M. (2009). Fifty- five- million- year history of oceanic subduction and exhumation at the
13
14 927 northern edge of the Caribbean plate (Sierra del Convento mélange, Cuba). *Journal of*
15
16 928 *metamorphic Geology*, 27(1), 19-40.
17
- 18 929 Leake, B. E., Woolley, A. R., Arps, C. E., Birch, W. D., Gilbert, M. C., Grice, J. D., Hawthorne, F.
19
20 930 C., Kato, A., Kisch, H. J., & Krivovichev, V. G. (1997). Report. Nomenclature of
21
22 931 amphiboles: report of the subcommittee on amphiboles of the international mineralogical
23
24 932 association commission on new minerals and mineral names. *Mineralogical Magazine*, 61(2),
25
26 933 295-321.
27
28
29
30
- 31 934 Leitch, E. (1975). Plate tectonic interpretation of the Paleozoic history of the New England Fold Belt.
32
33 935 *Geological Society of America Bulletin*, 86(1), 141-144.
34
- 35 936 Li, J.-L., Klemd, R., Gao, J., & John, T. (2016). Poly-cyclic metamorphic evolution of eclogite:
36
37 937 evidence for multistage burial–exhumation cycling in a subduction channel. *Journal of*
38
39 938 *Petrology*, 57(1), 119-146.
40
41
- 42 939 Li, P., Rosenbaum, G., Yang, J. H., & Hoy, D. (2015). Australian- derived detrital zircons in the
43
44 940 Permian- Triassic Gympie terrane (eastern Australia): Evidence for an autochthonous origin.
45
46 941 *Tectonics*, 34(5), 858-874.
47
48
- 49 942 Liati, A., Theye, T., Fanning, C. M., Gebauer, D., & Rayner, N. (2016). Multiple subduction cycles in
50
51 943 the Alpine orogeny, as recorded in single zircon crystals (Rhodope zone, Greece). *Gondwana*
52
53 944 *Research*, 29(1), 199-207.
54
- 55 945 Liferovich, R. P., & Mitchell, R. H. (2005). Composition and paragenesis of Na-, Nb-and Zr-bearing
56
57 946 titanite from Khibina, Russia, and crystal-structure data for synthetic analogues. *The*
58
59 947 *Canadian Mineralogist*, 43(2), 795-812.
60
61
62
63
64
65

- 1
2
3
4
5
6
7
8
9
10
11
12
13
14
15
16
17
18
19
20
21
22
23
24
25
26
27
28
29
30
31
32
33
34
35
36
37
38
39
40
41
42
43
44
45
46
47
48
49
50
51
52
53
54
55
56
57
58
59
60
61
62
63
64
65
- 948 Manton, R. J., Buckman, S., Nutman, A. P., Bennett, V. C., & Belousova, E. A. (2017). U- Pb- Hf-
949 REE- Ti zircon and REE garnet geochemistry of the Cambrian Attunga eclogite, New
950 England Orogen, Australia: Implications for continental growth along eastern Gondwana.
951 *Tectonics*, 36(8), 1580-1613.
- 952 Marmo, B., Clarke, G., & Powell, R. (2002). Fractionation of bulk rock composition due to
953 porphyroblast growth: effects on eclogite facies mineral equilibria, Pam Peninsula, New
954 Caledonia. *Journal of metamorphic Geology*, 20(1), 151-165.
- 955 Martin, L. A., Rubatto, D., Brovarone, A. V., & Hermann, J. (2011). Late Eocene lawsonite-eclogite
956 facies metasomatism of a granulite sliver associated to ophiolites in Alpine Corsica. *Lithos*,
957 125(1-2), 620-640.
- 958 Moresi, L., Betts, P., Miller, M., & Cayley, R. (2014). Dynamics of continental accretion. *Nature*,
959 508(7495), 245-248.
- 960 Och, D., Leitch, E., Caprarelli, G., & Watanabe, T. (2003). Blueschist and eclogite in tectonic
961 melange, port macquarie, new south wales, australia.
- 962 Och, D., Zwingmann, H., Philips, G., & Leitch, E. (2010). K-Ar dating of serpentinitisation using
963 fuchsite mica: the Rocky Beach metamorphic melange, PORT MACQUARIE.
- 964 Och, D. J. (2007). *Eclogite, serpentinite, mélangé and mafic intrusive rocks: manifestation of long-*
965 *lived Palaeozoic convergent margin activity, Port Macquarie, eastern Australia.*
- 966 Park, C., Song, Y., Kang, I.-M., Shim, J., Chung, D., & Park, C.-S. (2017). Metasomatic changes
967 during periodic fluid flux recorded in grandite garnet from the Weondong W-skarn deposit,
968 South Korea. *Chemical Geology*, 451, 135-153.
- 969 Paton, C., Hellstrom, J., Paul, B., Woodhead, J., & Hergt, J. (2011). Iolite: Freeware for the
970 visualisation and processing of mass spectrometric data. *Journal of Analytical Atomic*
971 *Spectrometry*, 26(12), 2508-2518.
- 972 Phillips, D., & Harris, J. (2008). Provenance studies from $^{40}\text{Ar}/^{39}\text{Ar}$ dating of mineral inclusions in
973 diamonds: Methodological tests on the Orapa kimberlite, Botswana. *Earth and Planetary*
974 *Science Letters*, 274(1), 169-178.

- 1
2
3
4
5
6
7
8
9
10
11
12
13
14
15
16
17
18
19
20
21
22
23
24
25
26
27
28
29
30
31
32
33
34
35
36
37
38
39
40
41
42
43
44
45
46
47
48
49
50
51
52
53
54
55
56
57
58
59
60
61
62
63
64
65
- 975 Phillips, G., Landenberger, B., & Belousova, E. (2011). Building the New England Batholith, eastern
976 Australia—Linking granite petrogenesis with geodynamic setting using Hf isotopes in zircon.
977 *Lithos*, 122(1-2), 1-12.
- 978 Phillips, G., & Offler, R. (2011). Contrasting modes of eclogite and blueschist exhumation in a
979 retreating subduction system: The Tasmanides, Australia. *Gondwana Research*, 19(3), 800-
980 811.
- 981 Phillips, G., Offler, R., Rubatto, D., & Phillips, D. (2015). High- pressure metamorphism in the
982 southern New England Orogen: Implications for long- lived accretionary orogenesis in
983 eastern Australia. *Tectonics*, 34(9), 1979-2010.
- 984 Phillips, G., Wilson, C. J., Phillips, D., & Szczepanski, S. K. (2007). Thermochronological
985 (40Ar/39Ar) evidence of Early Palaeozoic basin inversion within the southern Prince Charles
986 Mountains, East Antarctica: implications for East Gondwana. *Journal of the Geological
987 Society*, 164(4), 771-784.
- 988 Pourteau, A., Scherer, E. E., Schorn, S., Bast, R., Schmidt, A., & Ebert, L. (2019). Thermal evolution
989 of an ancient subduction interface revealed by Lu–Hf garnet geochronology, Halilbağ
990 Complex (Anatolia). *Geoscience Frontiers*, 10(1), 127-148.
- 991 Powell, R., & Holland, T. (1988). An internally consistent dataset with uncertainties and correlations:
992 3. Applications to geobarometry, worked examples and a computer program. *Journal of
993 metamorphic Geology*, 6(2), 173-204.
- 994 Putlitz, B., Cosca, M., & Schumacher, J. (2005). Prograde mica 40Ar/39Ar growth ages recorded in
995 high pressure rocks (Syros, Cyclades, Greece). *Chemical Geology*, 214(1-2), 79-98.
- 996 Roberts, J., & James, L. (2010). Stratigraphic relationships of Carboniferous volcanogenic
997 successions in the Clifton–Carroll block and Werrie syncline, northern Tamworth Belt,
998 southern New England Orogen. *Australian Journal of Earth Sciences*, 57(2), 193-205.
- 999 Roda, M., Zucali, M., Regorda, A., & Iole Spalla, M. (2019). Formation and evolution of a
1000 subduction-related mélange: The example of the Rocca Canavese Thrust Sheets (Western
1001 Alps). *Geological Society of America Bulletin*.

- 1002 Rodriguez, J., Cosca, M., Ibarguchi, J. G., & Dallmeyer, R. (2003). Strain partitioning and
1 preservation of $^{40}\text{Ar}/^{39}\text{Ar}$ ages during Variscan exhumation of a subducted crust (Malpica–
2 1003 Tui complex, NW Spain). *Lithos*, 70(3-4), 111-139.
3
4 1004
5
6 1005 Rubatto, D., Regis, D., Hermann, J., Boston, K., Engi, M., Beltrando, M., & McAlpine, S. R. (2011).
7
8 1006 Yo-yo subduction recorded by accessory minerals in the Italian Western Alps. *Nature*
9
10
11 1007 *Geoscience*, 4(5), 338.
12
13 1008 Sano, S., Offler, R., Hyodo, H., & Watanabe, T. (2004). Geochemistry and chronology of tectonic
14
15 1009 blocks in serpentinite mélangé of the southern New England Fold Belt, NSW, Australia.
16
17 1010
18 *Gondwana Research*, 7(3), 817-831.
19
20 1011 Schumacher, R., Rötzler, K., & Maresch, W. (1999). Subtle oscillatory zoning in garnet from regional
21
22 1012 metamorphic phyllites and mica schists, western Erzgebirge, Germany. *The Canadian*
23
24 1013 *Mineralogist*, 37(2), 381-403.
25
26 1014 Seifert, W. (2005). REE-, Zr-, and Th-rich titanite and associated accessory minerals from a kersantite
27
28 1015 in the Frankenwald, Germany. *Mineralogy and Petrology*, 84(3-4), 129-146.
29
30 1016 Seifert, W., & Kramer, W. (2003). Accessory titanite: an important carrier of zirconium in
31
32 1017 lamprophyres. *Lithos*, 71(1), 81-98.
33
34 1018 Shaw, S., & Flood, R. (1981). The New England Batholith, eastern Australia: geochemical variations
35
36 1019 in time and space. *Journal of Geophysical Research: Solid Earth*, 86(B11), 10530-10544.
37
38 1020 Shreve, R. L., & Cloos, M. (1986). Dynamics of sediment subduction, melange formation, and prism
39
40 1021 accretion. *Journal of Geophysical Research: Solid Earth*, 91(B10), 10229-10245.
41
42 1022 Spandler, C., Hammerli, J., Sha, P., Hilbert-Wolf, H., Hu, Y., Roberts, E., & Schmitz, M. (2016).
43
44 1023 MKED1: a new titanite standard for in situ analysis of Sm–Nd isotopes and U–Pb
45
46 1024 geochronology. *Chemical Geology*, 425, 110-126.
47
48 1025 Spear, F. S. (1988). Metamorphic fractional crystallization and internal metasomatism by diffusional
49
50 1026 homogenization of zoned garnets. *Contributions to Mineralogy and Petrology*, 99(4), 507-
51
52 1027 517.
53
54
55
56
57
58
59
60
61
62
63
64
65

- 1028 Spencer, K., Hacker, B., Kylander-Clark, A., Andersen, T., Cottle, J., Stearns, M., Poletti, J., &
1
21029 Seward, G. (2013). Campaign-style titanite U–Pb dating by laser-ablation ICP: Implications
3
41030 for crustal flow, phase transformations and titanite closure. *Chemical Geology*, 341, 84-101.
5
61031 Stöckhert, B., & Gerya, T. V. (2005). Pre- collisional high pressure metamorphism and nappe
7
81032 tectonics at active continental margins: A numerical simulation. *Terra Nova*, 17(2), 102-110.
9
10
111033 Tamblyn, R., Hand, M., Kelsey, D., Anczkiewicz, R., & Och, D. (2019). Subduction and
12
131034 accumulation of lawsonite eclogite and garnet blueschist in eastern Australia. *Journal of*
14
151035 *metamorphic Geology*.
16
17
181036 Tamblyn, R., Zack, T., Schmitt, A., Hand, M., Kelsey, D., Morrissey, L., Pabst, S., & Savov, I.
19
201037 (2019). Blueschist from the Mariana forearc records long-lived residence of material in the
21
221038 subduction channel. *Earth and Planetary Science Letters*, 519, 171-181.
23
24
251039 Tsujimori, T., & Ernst, W. (2014). Lawsonite blueschists and lawsonite eclogites as proxies for
26
271040 palaeo- subduction zone processes: a review. *Journal of metamorphic Geology*, 32(5), 437-
28
291041 454.
30
311042 Tsujimori, T., Sisson, V. B., Liou, J. G., Harlow, G. E., & Sorensen, S. S. (2006). Very-low-
32
331043 temperature record of the subduction process: A review of worldwide lawsonite eclogites.
34
351044 *Lithos*, 92(3), 609-624.
36
37
381045 Vermeesch, P. (2018). IsoplotR: a free and open toolbox for geochronology. *Geoscience Frontiers*,
39
401046 9(5), 1479-1493.
41
421047 Viete, D. R., Hacker, B. R., Allen, M. B., Seward, G. G., Tobin, M. J., Kelley, C. S., Cinque, G., &
43
441048 Duckworth, A. R. (2018). Metamorphic records of multiple seismic cycles during subduction.
45
461049 *Science advances*, 4(3), eaaq0234.
47
48
491050 Vuorinen, J. H., & Hålenius, U. (2005). Nb-, Zr-and LREE-rich titanite from the Alnö alkaline
50
511051 complex: crystal chemistry and its importance as a petrogenetic indicator. *Lithos*, 83(1-2),
52
531052 128-142.
54
55
561053 Warren, C., Sherlock, S., & Kelley, S. (2011). Interpreting high-pressure phengite $^{40}\text{Ar}/^{39}\text{Ar}$
57
581054 laserprobe ages: an example from Saih Hatat, NE Oman. *Contributions to Mineralogy and*
59
601055 *Petrology*, 161(6), 991-1009.
61
62
63
64
65

- 1056 Wei, C., & Clarke, G. (2011). Calculated phase equilibria for MORB compositions: a reappraisal of
1
21057 the metamorphic evolution of lawsonite eclogite. *Journal of metamorphic Geology*, 29(9),
3
41058 939-952.
5
61059 White, R., Powell, R., & Holland, T. (2007). Progress relating to calculation of partial melting
7
81060 equilibria for metapelites. *Journal of metamorphic Geology*, 25(5), 511-527.
9
10
111061 Woodhead, J. D., & Hergt, J. M. (2001). Strontium, neodymium and lead isotope analyses of NIST
12
131062 glass certified reference materials: SRM 610, 612, 614. *Geostandards Newsletter*, 25(2- 3),
14
151063 261-266.
16
17
181064 Zack, T., & Hogmalm, K. J. (2016). Laser ablation Rb/Sr dating by online chemical separation of Rb
19
201065 and Sr in an oxygen-filled reaction cell. *Chemical Geology*, 437, 120-133.
21

221066

23

241067

25

261068

27

28

291069

Declarations

30

311070

32

331071

Funding

34

351072

This research in part was supported by an Australian Research Council grant (DP160104637). The

36

371073

contribution of Jack Gillespie was supported by an Australian Research Council Discovery Project

38

39

401074

(DP190103849). Part of this research was undertaken using SEM instrumentation (ARC

41

421075

LE190100176, LE140100150) at the John de Laeter Center, Curtin University. Renée Tamblyn

43

441076

acknowledges support from the University of Adelaide in the form of the Aldermann Kleeman

45

461077

travel scholarship and an Australian Postgraduate Award.

47

48

491078

Conflicts of interest/competing interests

50

511079

The authors declare no conflicts of interest or competing interests

52

531080

Availability of data and material

54

551081

All data presented in this manuscript can be found in the supplementary materials

56

57

581082

Code availability

59

601083

Not applicable

61

62

63

64

65

1084 *Figure captions*

1
2
3
4
5
6
7
8
9
10
11
12
13
14
15
16
17
18
19
20
21
22
23
24
25
26
27
28
29
30
31
32
33
34
35
36
37
38
39
40
41
42
43
44
45
46
47
48
49
50
51
52
53
54
55
56
57
58
59
60
61
62
63
64
65

1085
1086 Figure 1: a) Simplified map of eastern Australia (east of the Tasman line) showing the main eastward-
1087 younging orogens. The SNEO is indicated in the black box. b) Geological map of the SNEO, showing
1088 other high-pressure rock localities and indicating the location of Port Macquarie in the black box.
1089 PMFS: Peel Manning Fault System. c) Geological map of Rocky Beach at Port Macquarie, showing
1090 the high-pressure *mélange* encased in serpentinite, modified from Och et al. (2003).

1091
1092 Figure 2: Mineral textural relationships in the Port Macquarie eclogite. a) Eclogite in outcrop,
1093 showing coarse-grained garnet, phengite and lawsonite with patches of omphacite, which is partially
1094 retrogressed by glaucophane. b) Photomicrograph showing the porphyroblastic nature of garnet,
1095 lawsonite and omphacite, in a finer-grained phengite and titanite matrix. c) Stage 2 retrograde features
1096 of the eclogite, showing chlorite replacement of garnet and glaucophane replacement of omphacite. d)
1097 Garnet 2 enclosing a pre-existing garnet 1 porphyroblast. Boundary between the stage 1 garnet and
1098 stage 2 garnet is shown by a white dashed line. The boundary between the two garnet domains
1099 contains entrapped chlorite and omphacite inclusions. e) Radial fractures surrounding a quartz
1100 inclusion in the outermost part garnet 1. f) Large lawsonite porphyroblast, with an inclusion-rich
1101 euhedral crystal (lawsonite 1) which is overgrown by a rim (lawsonite 2). The new lawsonite growth
1102 contains inclusions of garnet 2 that developed on the margin of the older lawsonite, as well as stage 2
1103 glaucophane and titanite. Abbreviations: O: Omphacite; Law: Lawsonite; Phe: Phengite; Ttn: Titanite;
1104 G: Garnet; Chl: Chlorite; Gl: Glaucophane; Stlp: Stilpnomelane; Q: Quartz.

1105
1106 Figure 3: Schematic interpretation of the petrologic evolution of the lawsonite eclogite. a) Prograde-
1107 peak stage 1 burial: garnet cores nucleate and as garnet 1 grows it entraps prograde mineralogy and
1108 inclusion trails. Lawsonite porphyroblasts grow and entrap prograde minerals. b) Retrograde 1: garnet
1109 is partially consumed by chlorite, and glaucophane forms at the expense of omphacite. c) Prograde-
1110 peak 2: garnet forms new rims (garnet 2). In rare instances stage 2 garnet overgrows stage 1

1111 lawsonite. Phengite recrystallises in the matrix with coarse-grained titanite during deformation. d)

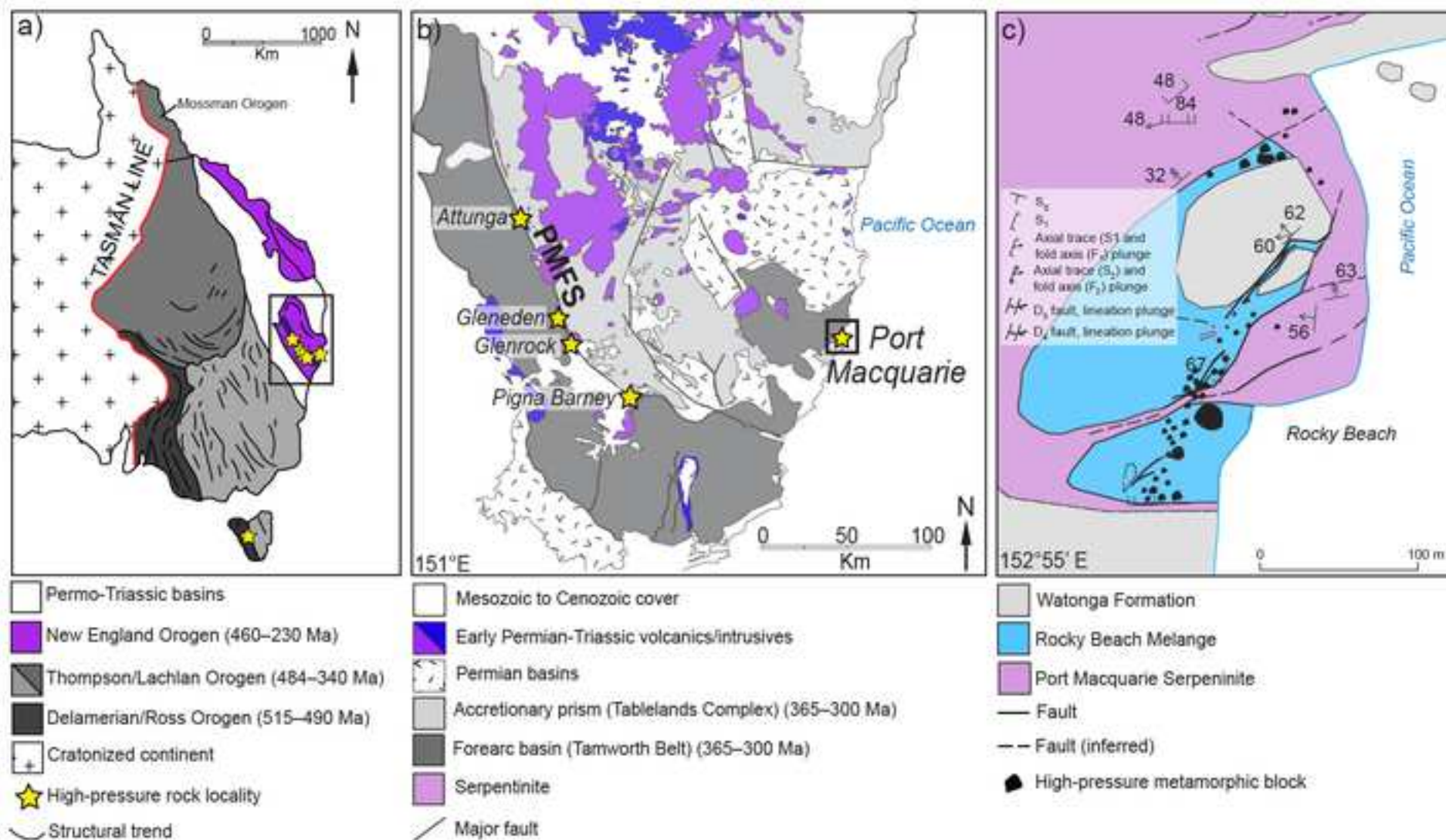
1
21112 Stage 2 retrograde: garnet is partially replaced by chlorite and omphacite is partially replaced by
3
41113 glaucophane. There is minor growth of lawsonite.
5
61114
7
8
91115 Figure 4: Representative EPMA traverse of garnet, showing the proportions of end-members and X_{Fe} .

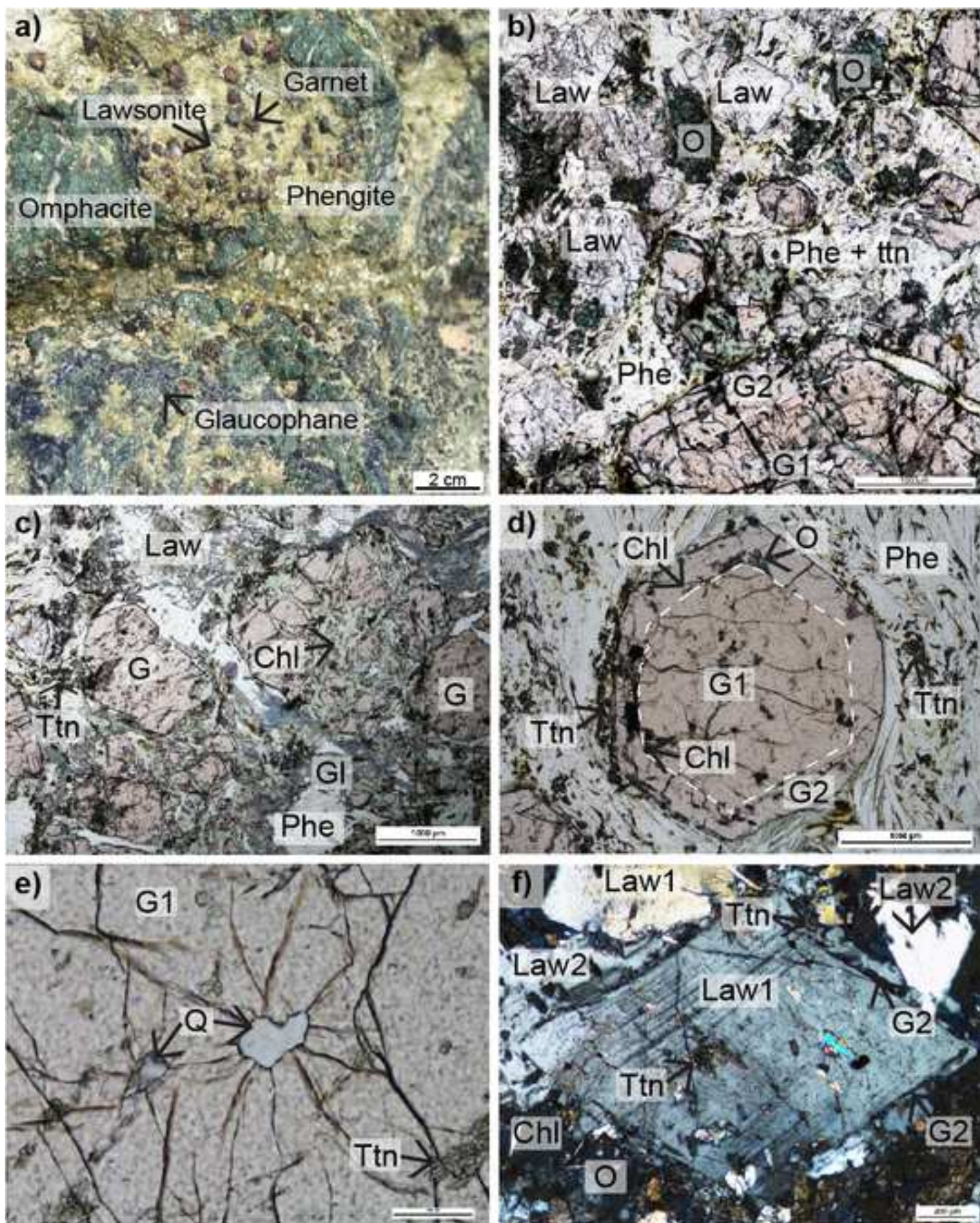
10
111116 a) Traverse across entire garnet porphyroblast, showing a prograde bell-shaped zoning profile. b)
12
131117 Traverse across stage 1 garnet to stage 2 garnet, showing a step decrease in X_{Fe} and increase in
14
151118 spessartine content.
16
17
181119
19
201120 Figure 5: EPMA element maps of garnet, the white dashed line shows the interpreted boundary
21
221121 between garnet 1 and garnet 2. a) Garnet porphyroblasts with prograde zoning in Mn, along with
23
24
251122 several oscillatory rings in the stage 2 rim. Zoning in Fe and Mg show garnet 2 as a marked outer ring
26
271123 with elevated X_{Mg} . Subset maps are marked in grey boxes. b) Compositional oscillations in the garnet
28
291124 2 which define smaller hexagonal garnet crystals that nucleated on the older garnet 1 rim. c) Complex
30
311125 Mn zoning patterns and a marked X_{Mg} increase in the outer garnet rim. Embayments and subsequent
32
33
341126 overgrowths are highlighted in the Mn oscillations, with correlate with Ca oscillations. Late chlorite
35
361127 replaces garnet. The boundary between garnet 1 and garnet 2 contains Mn-rich chlorite inclusions.
37
381128
39
401129 Figure 6: EPMA maps across transition from garnet 1 to garnet 2 and into matrix phengite.
41
42
431130 White/black dashed line indicates the boundaries of garnet 1 and garnet 2. Solid white/black line
44
451131 indicates the boundaries of phengite included in garnet.
46
471132
48
491133 Figure 7: Mineral compositions of omphacite, phengite, chlorite and titanite measured by EPMA. a)
50
51
521134 Omphacite analyses from inclusions in garnet and omphacite porphyroblasts in the matrix. b)
53
541135 Phengite analyses showing increasing Si, Fe and Mg component from core to rim, and decreasing Na
55
561136 content. c) Chlorite analyses from stage 1 chlorite, from the boundary between garnet 1 and garnet 2,
57
581137 and stage 2 chlorite, from the matrix. d) Titanite analyses showing elevated Al_2O_3 , FeO and F
59
60
61
62
63
64
65

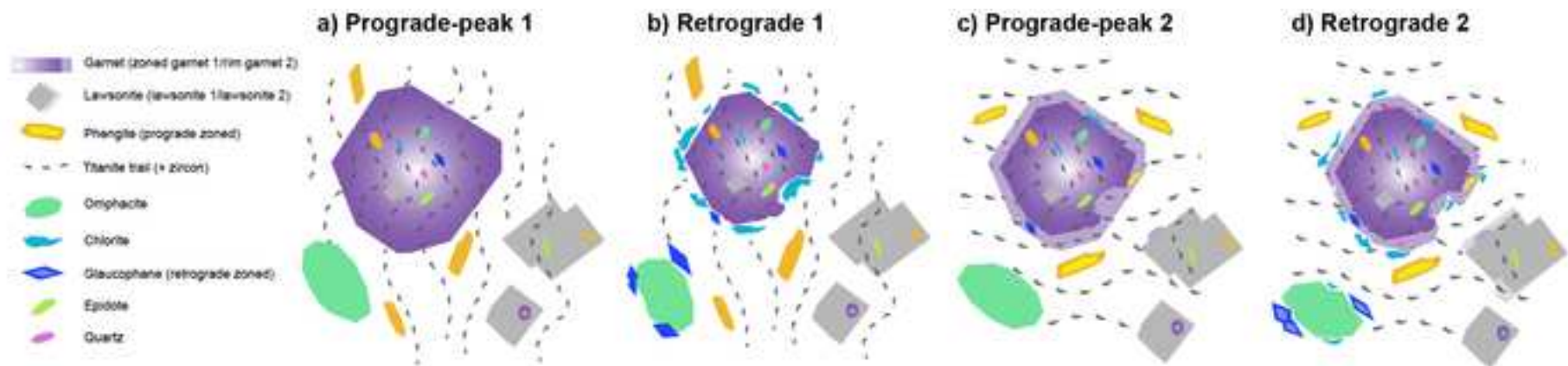
1138 contents with a positive correlation, suggesting increasing pressure during crystallization (e.g. Castelli
1
21139 & Rubatto, 2002).
3
41140
5
61141 Figure 8: a) Phase equilibrium model calculated with THERMOCALC, modified from Tamblyn et al.
7
81142 (2019a), calculated with garnet 1 and lawsonite 2 included in the bulk rock chemistry. Dashed thin
9
101143 grey lines indicate the position of solvi. Colour changes indicate changes in variance across fields. b)
11
121144 Model (a) showing the prograde assemblage and estimated garnet mode at stage 1 peak. Thick grey
13
141145 arrow indicates the interpreted P - T path of stage 1 prograde-peak. Abbreviations: Act: Actinolite, Bi:
15
161146 Biotite, Chl: Chlorite, Coe: Coesite, Ep: Epidote, G: Garnet, Gl: Glaucophane, Hb: Hornblende, Jd:
17
181147 Jadeite, Law: Lawsonite, O: Omphacite, Pa: Paragonite, Phe: Phengite, Pl: Plagioclase, Q: Quartz, Ta:
19
201148 Talc.
21
221149
23
241150 Figure 9: a) Phase equilibrium model calculated with THERMOCALC for the local rock composition
25
261151 with garnet 1 and lawsonite 1 removed, and water in excess. Dashed thin grey lines indicate the
27
281152 position of solvi. Colour changes indicate changes in variance across fields. Note the scale change
29
301153 from Figure 8. b) Model (a) showing the interpreted peak conditions of stage 1 peak from Figure 8b,
31
321154 and the interpreted stage 1 retrograde path in the thick grey arrow. Note these retrograde P - T
33
341155 conditions are considered the maximum possible pressures and temperatures obtained during
35
361156 retrogression. c) Model (a) showing the interpreted stage 2 prograde and peak assemblages, and
37
381157 mineral compositional isopleths. Thick grey arrow indicates the interpreted P - T path during stage 2
39
401158 prograde to peak. Abbreviations are listed in Figure 8.
41
421159
43
441160 Figure 10: a) Phase equilibrium model calculated with THERMOCALC for the local rock
45
461161 composition with garnet 1 and lawsonite 1 removed, and set water content. Dashed thin grey lines
47
481162 indicate the position of solvi. Colour changes indicate changes in variance across fields. Note the
49
501163 scale change from Figure 8. b) Model (a) showing a possible alternative path for stage 2 prograde,
51
521164 based on compositional isopleths from garnet 1, omphacite and phengite cores. Peak conditions
53
54
55
56
57
58
59
60
61
62
63
64
65

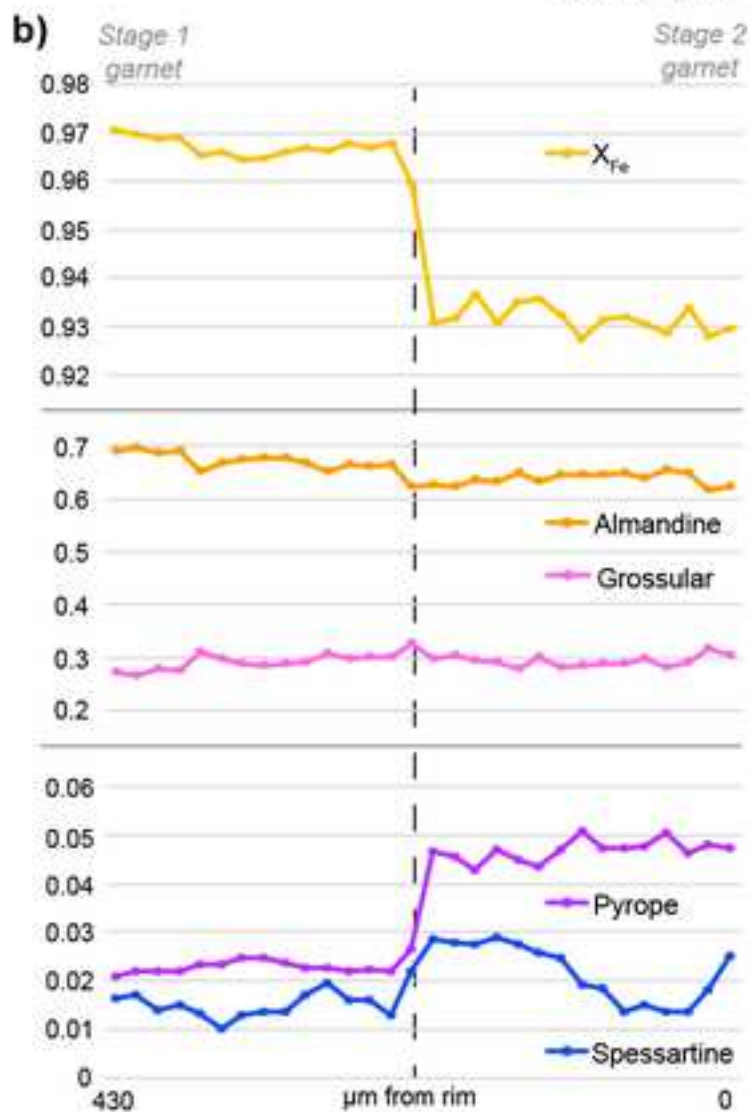
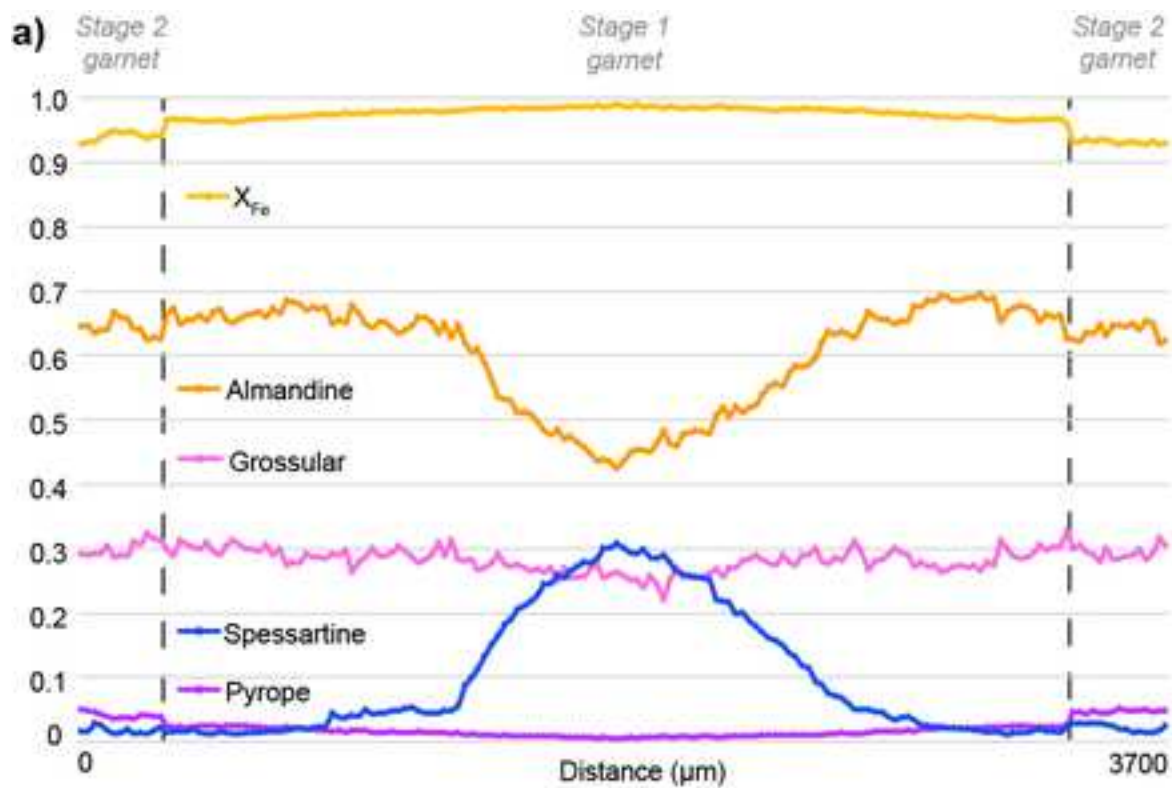
1165 remain the same. c) Model (a) showing the final stage 2 retrograde conditions reached, based on
1
21166 modal proportion isopleths. Abbreviations are listed in Figure 8.
3
41167
5
61168 Figure 11: Results of LA–ICP–MS U–Pb titanite geochronology and representative BSE images of
7
81169 analysed titanite grains. a) Terra–Wasserburg plot . b) Coarse-grained titanite in the rim of a stage 2
9
10
111170 lawsonite crystal (outlined in white dotted line) displaying a well-formed mesh-like intergrowth of
12
131171 exsolved zircon. c) Coarse titanite trails outlined in purple in the rims of stage 2 garnet, which is
14
151172 distinguished from the stage 1 garnet core by the black dotted line. d) Titanite grains rim a prograde
16
171173 zoned phengite, which has darker cores and brighter rims.
18
19
201174
21
221175 Figure 12: Step-heating Ar–Ar results from two phengite grains in the lawsonite eclogite.
23
241176
25
26
271177 Figure 13: In-situ LA–ICP–MS Rb–Sr geochronological results. a) Isochron constructed from
28
291178 analyses of phengite rims. b) Isochron constructed from analyses of phengite cores. c) Isochron using
30
31
321179 both phengite cores and rims. The isochrons produce similar ages within the uncertainties. d) Isotopic
33
341180 analyses of texturally intergrown titanite, which records the initial $^{87}\text{Sr}/^{86}\text{Sr}$ isotopic ratio. e) Isochron
35
361181 constructed from phengite rims and anchored with titanite analyses.
37
381182
39
40
411183 Figure 14: LA–ICP–MS Rb and Sr maps of phengite from the lawsonite eclogite. Maps are semi-
42
431184 quantitative. Phengites show Sr enrichments of all isotopes in their cores, and sometimes a slight Rb
44
451185 enrichment in their rims. These enrichments follow along cleavage planes of the phengite. The
46
471186 boundaries between these rims and cores are extremely sharp and well-defined. The Sr-rich mineral is
48
491187 titanite. The outline of phengite grains is shown in white. Rb-rich material without obvious grain
50
51
521188 boundaries traced is fine-grained phengite.
53
541189
55
56
571190 Figure 15: Summary of the P – T – t path of the lawsonite eclogite. Lu–Hf geochronology from
58
591191 lawsonite and garnet dates an earlier event during burial 1. Ar–Ar and Rb–Sr data from phengite, and
60
61
62
63
64
65

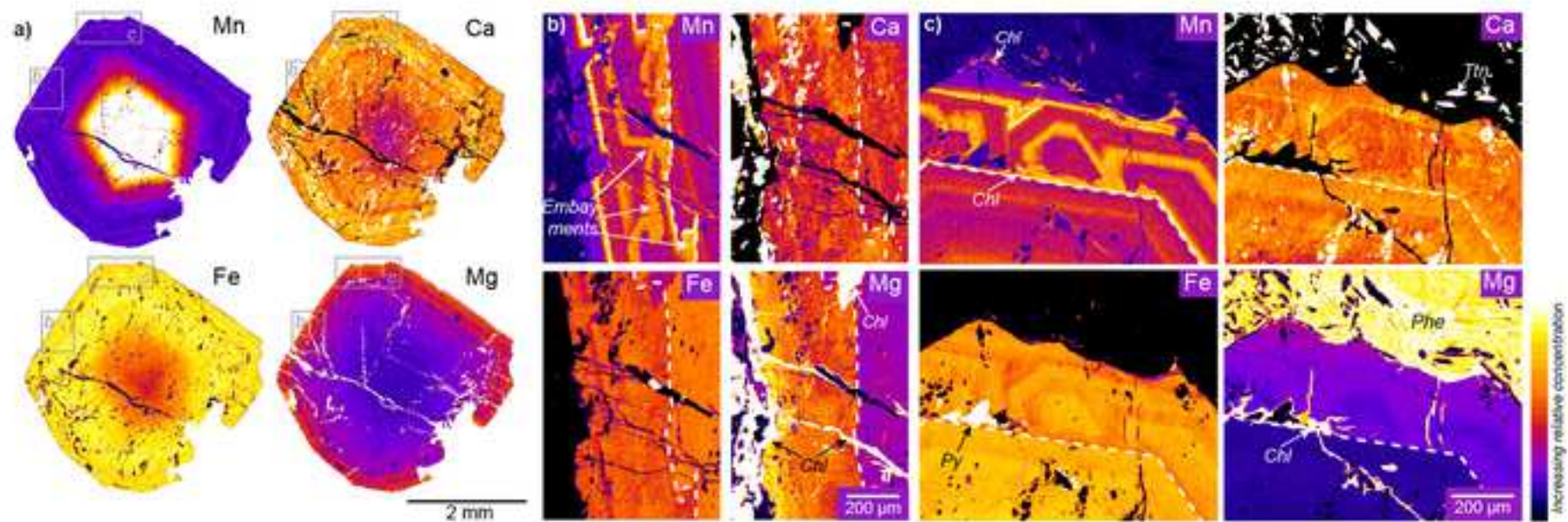
1192 U–Pb data from titanite, date a younger recrystallization event associated with reburial of the
1
21193 lawsonite eclogite within the subduction channel. This results in two hairpin P – T loops. While the
3
41194 exact timing of exhumation and P – T conditions reached between these two burial events is unknown,
5
61195 it must have occurred between approximately 485–465 Ma.
7
8
91196
10
111197
12
131198
14
151199
16
171200
18
191201
20
211202
22
231203
24
25
261204
27
281205
29
301206
31
321207
33
34
351208
36
371209
38
391210
40
411211
42
431212
44
451213
46
471214
48
491215
50
51
52
53
54
55
56
57
58
59
60
61
62
63
64
65

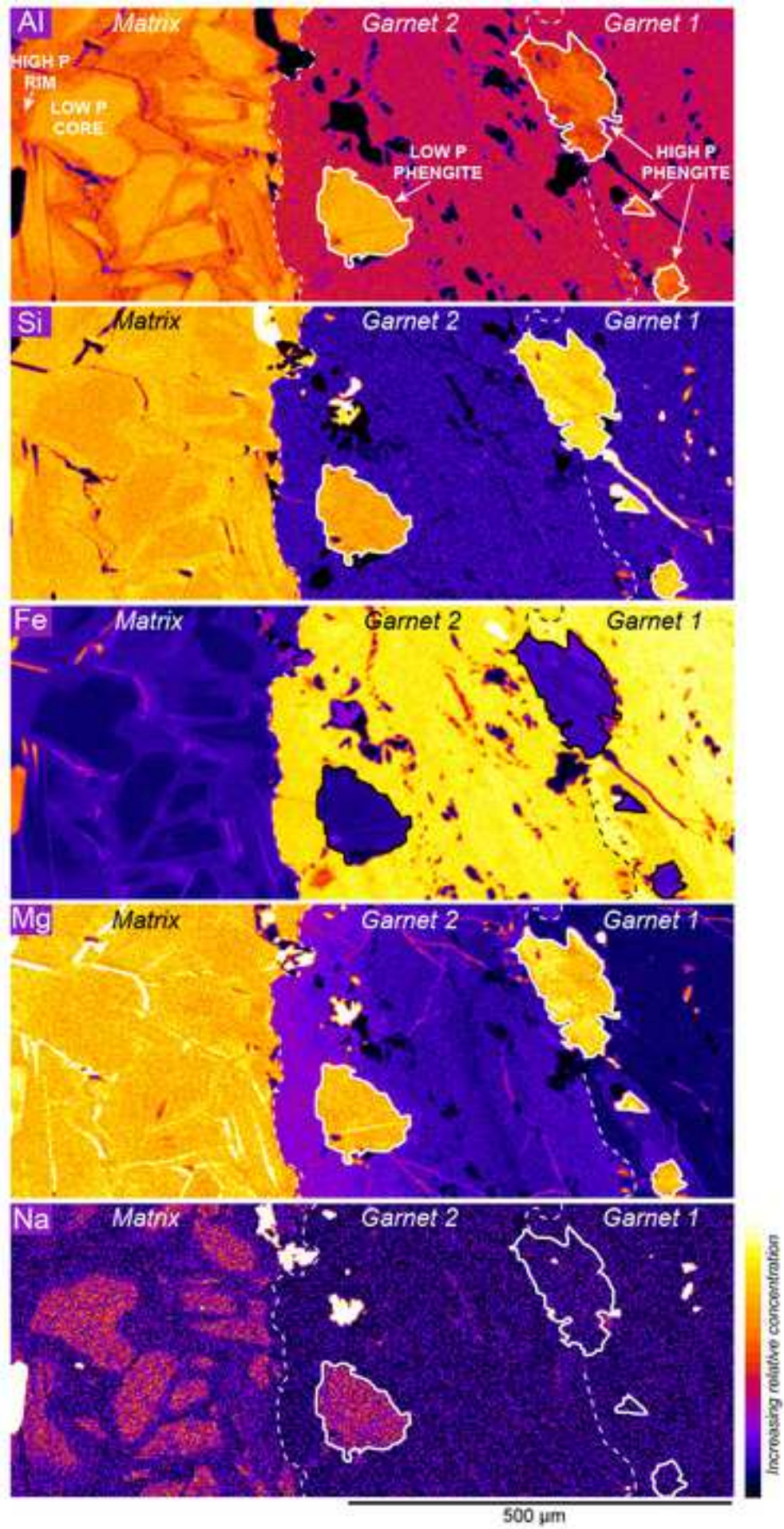


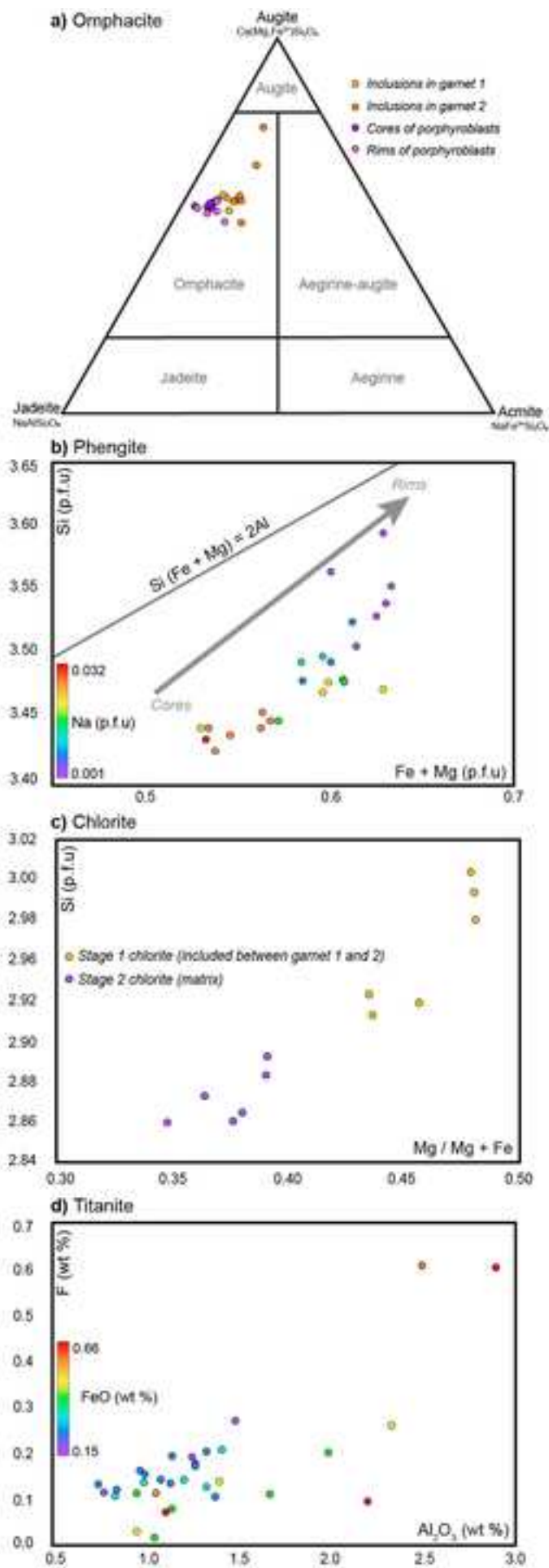


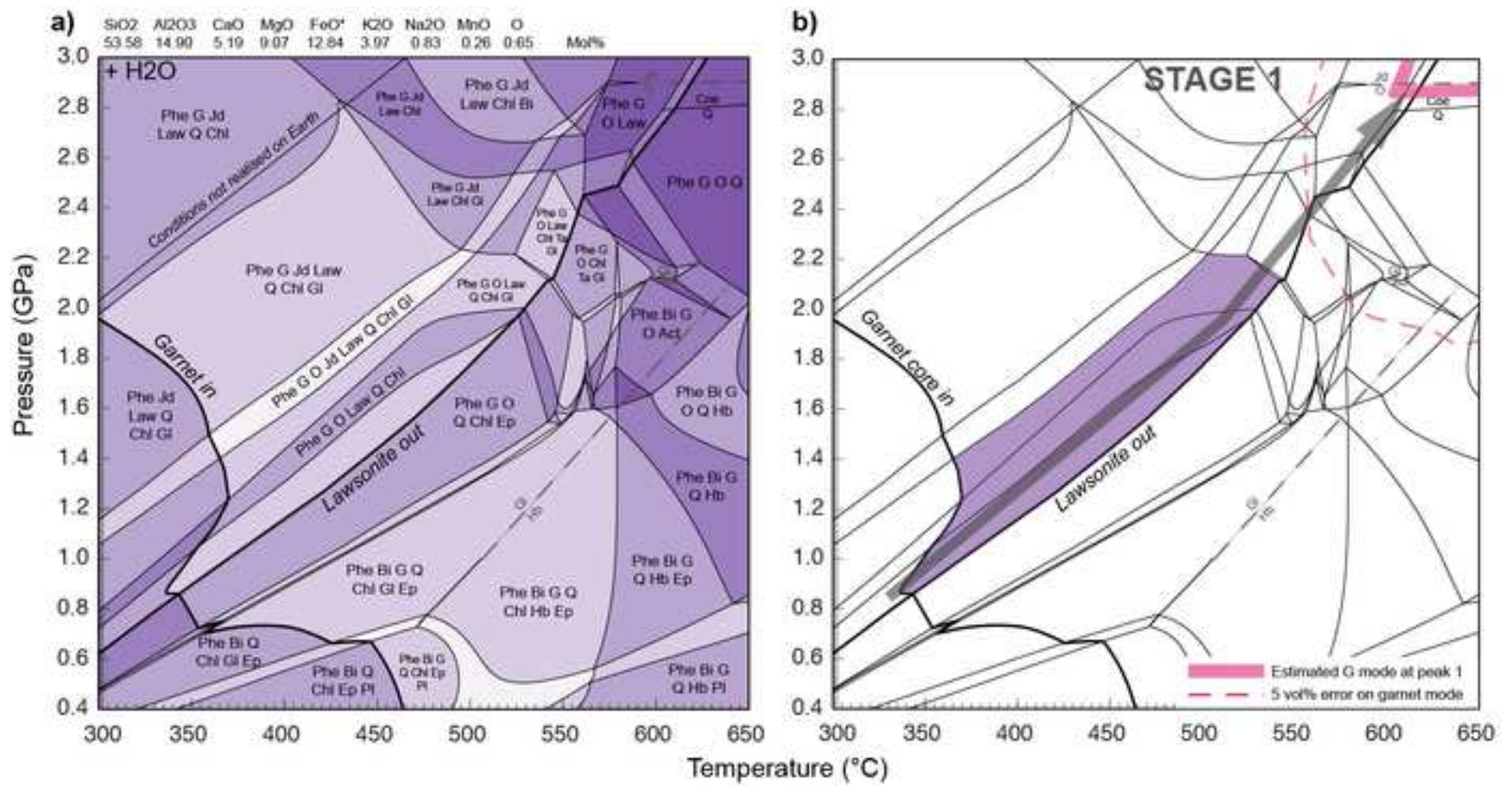


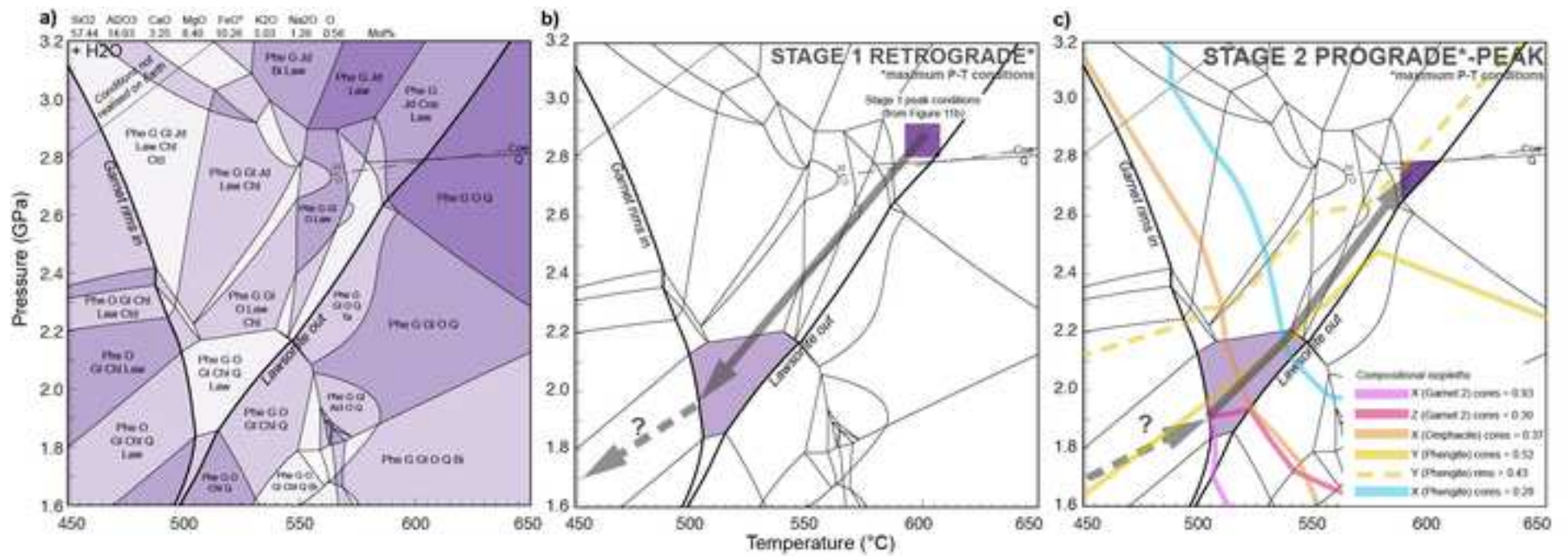


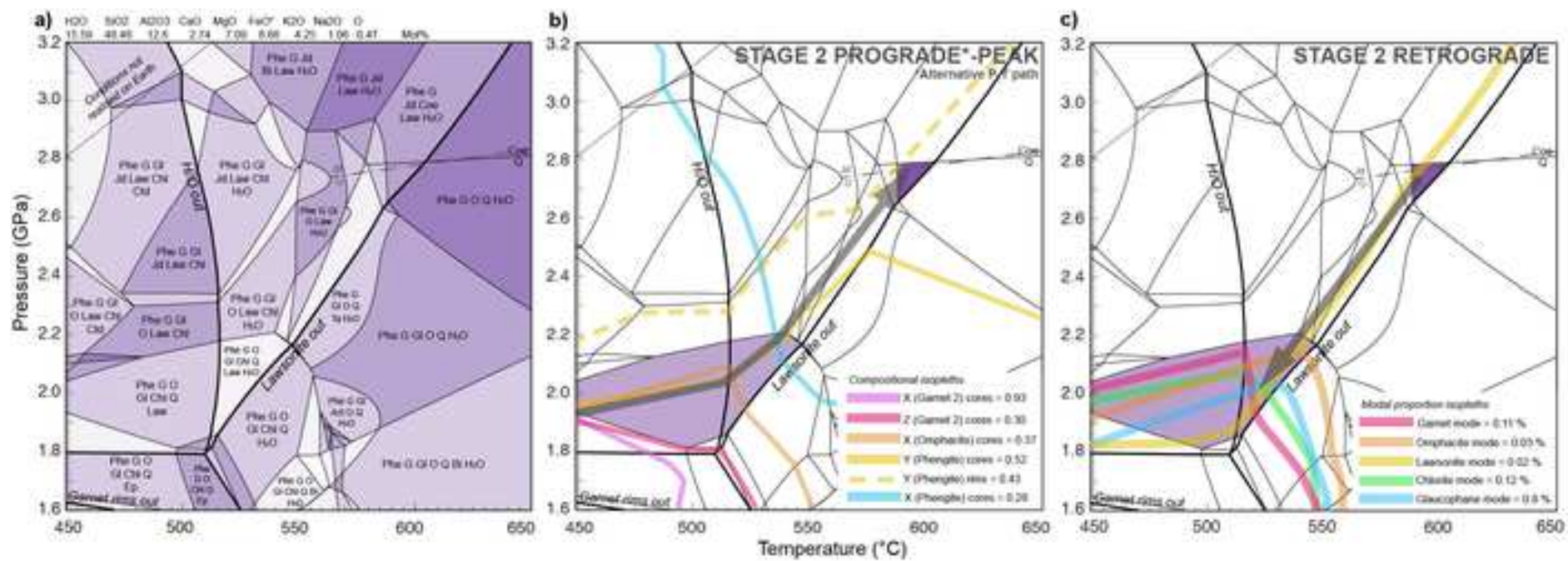


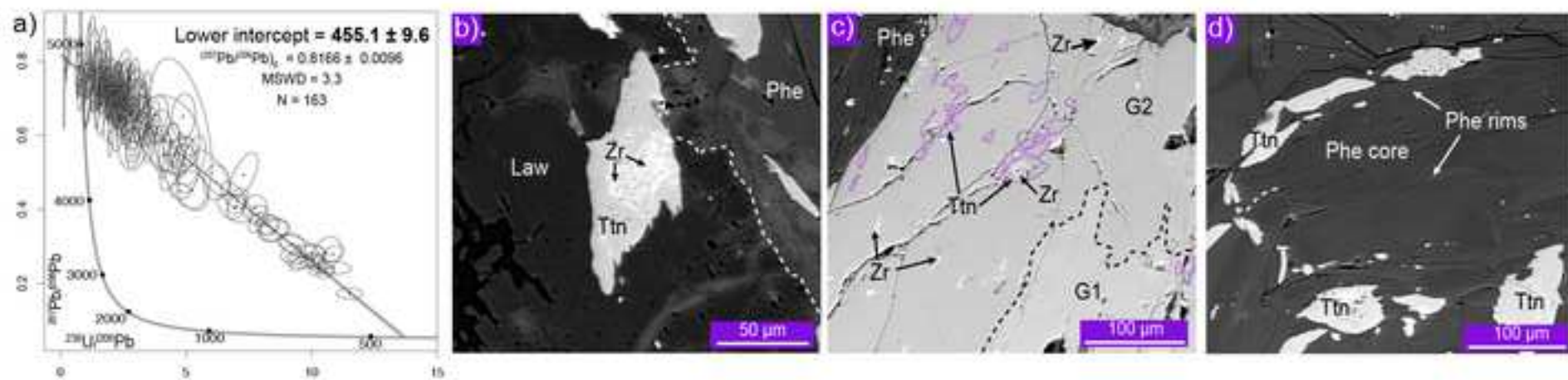


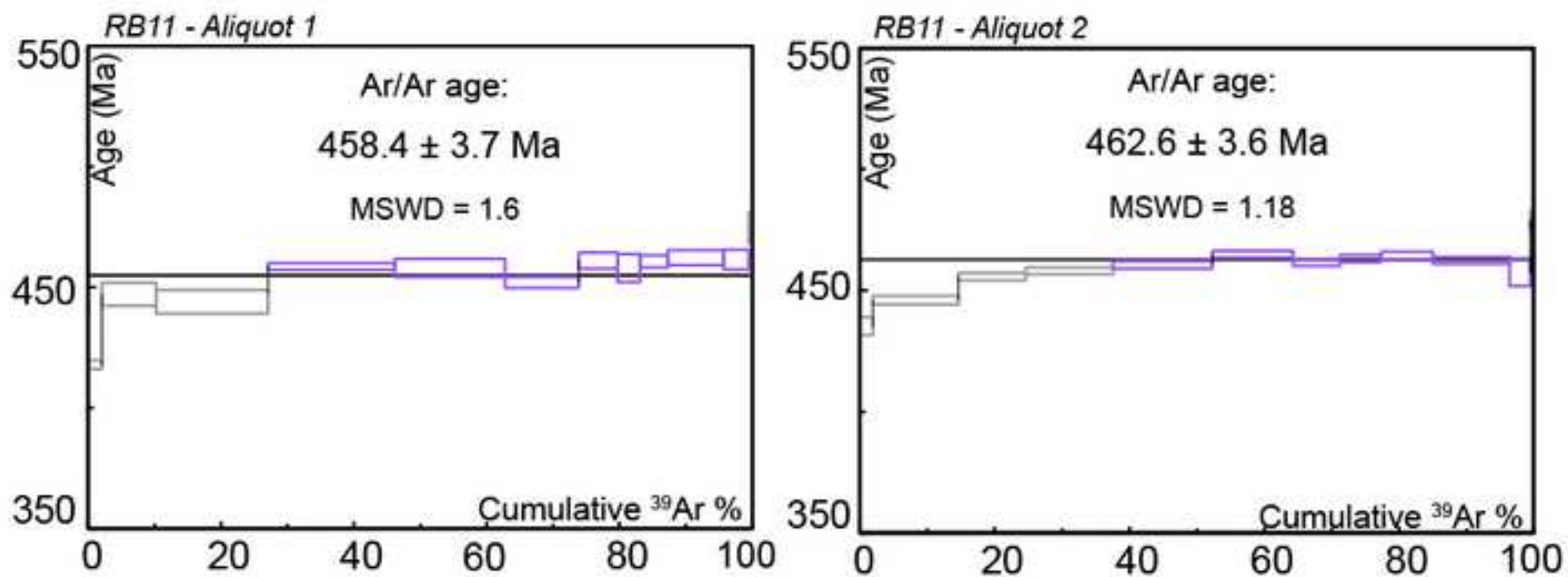


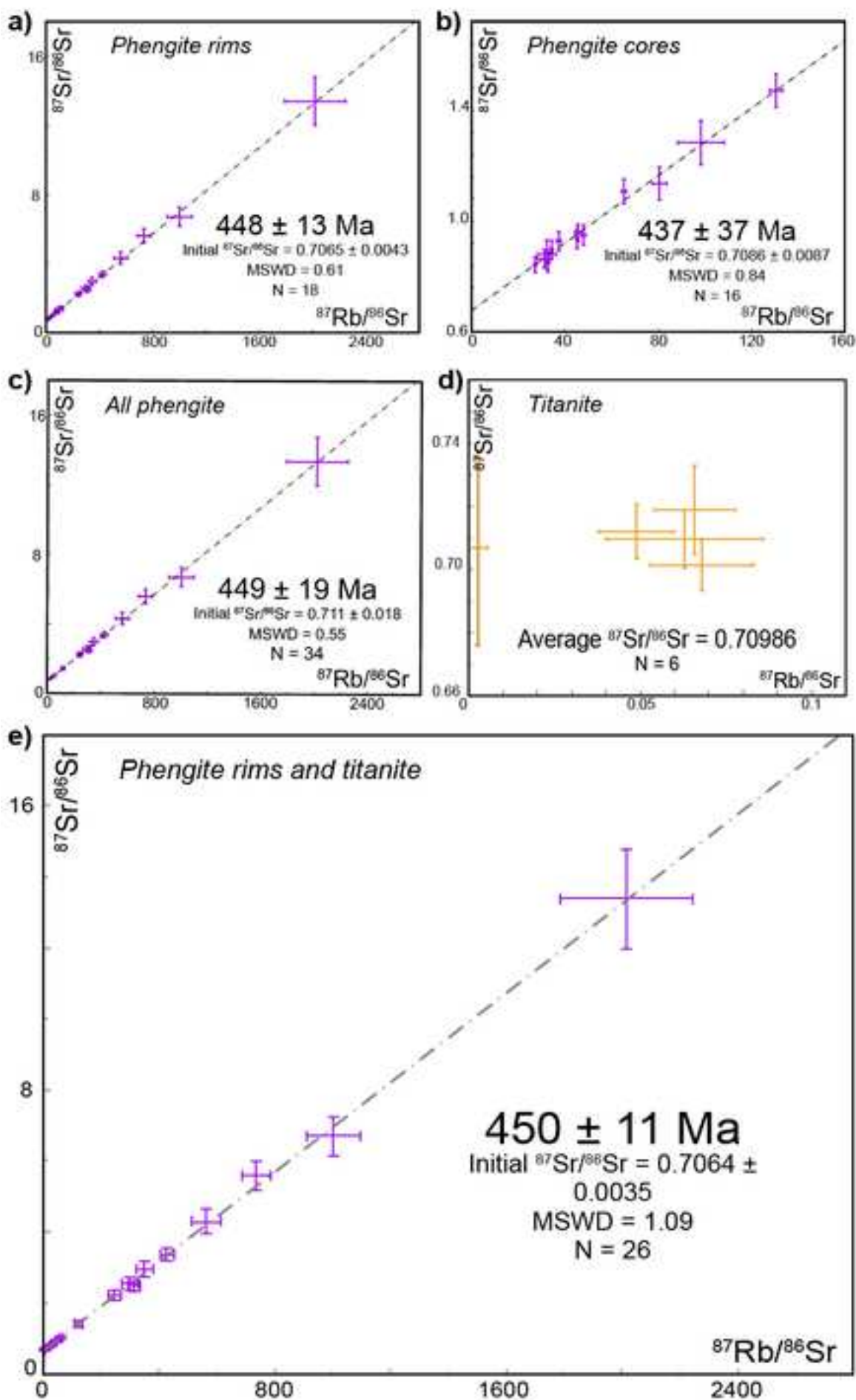




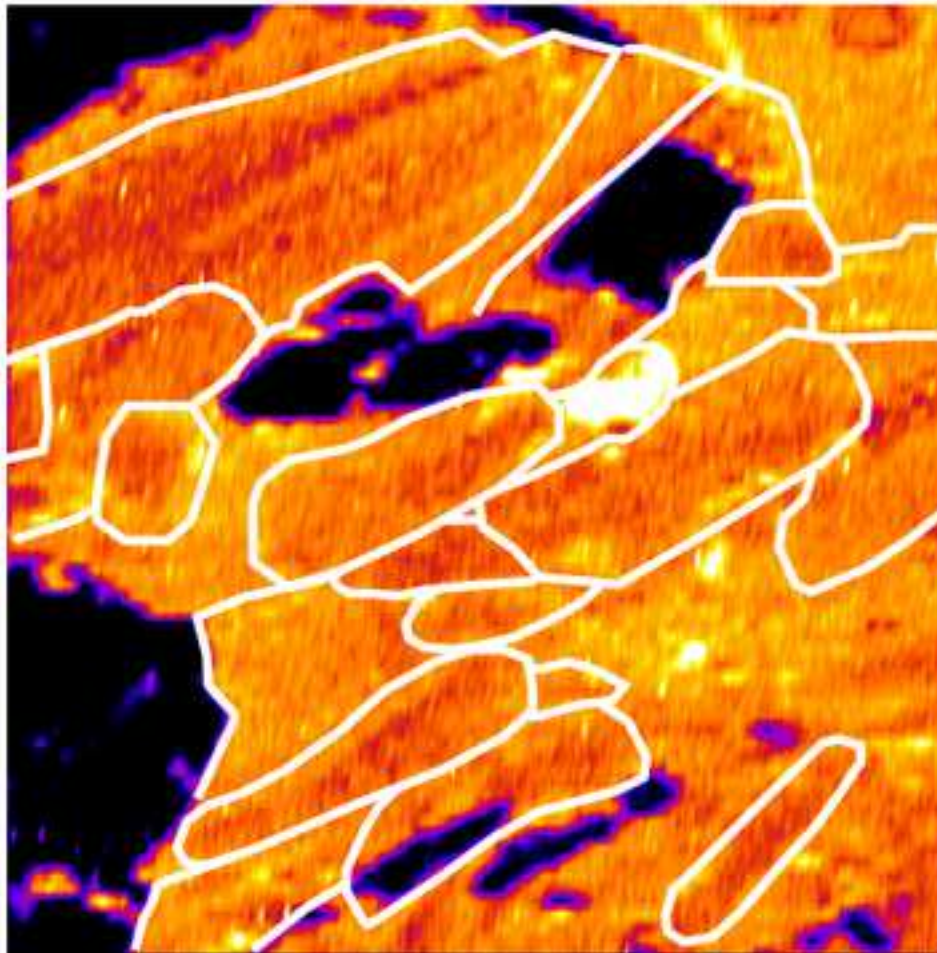




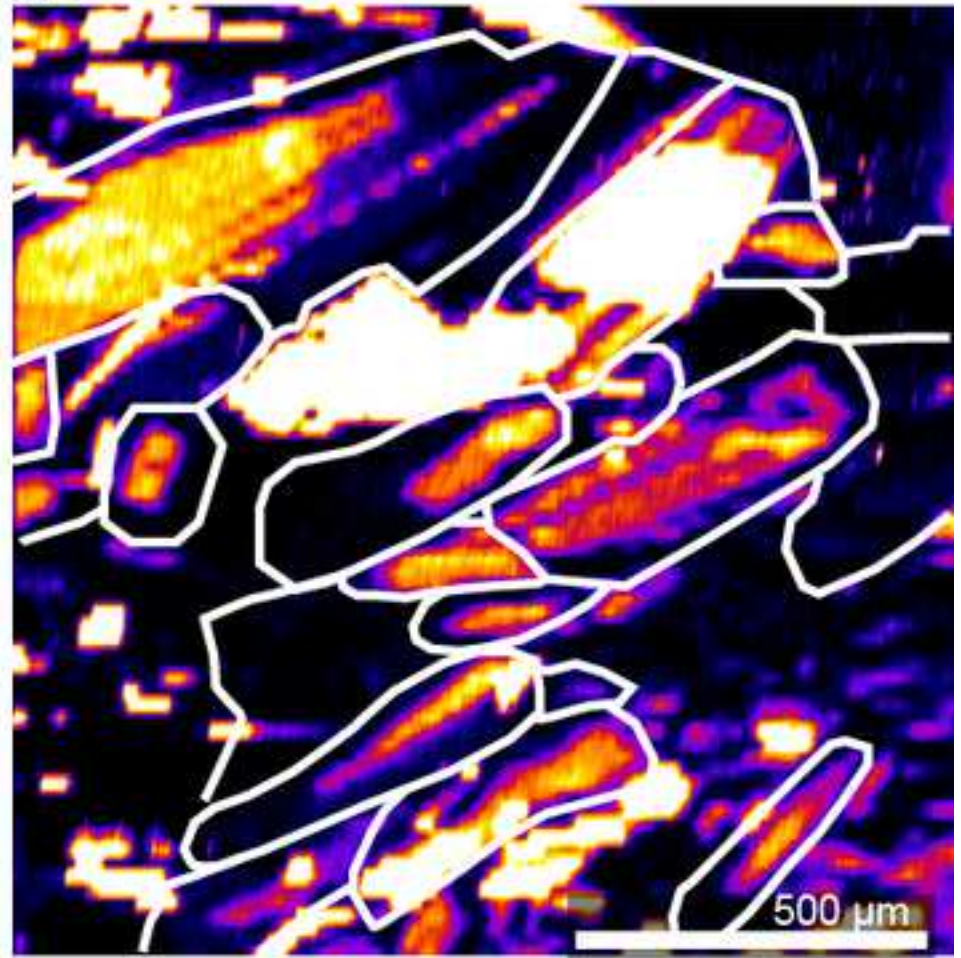


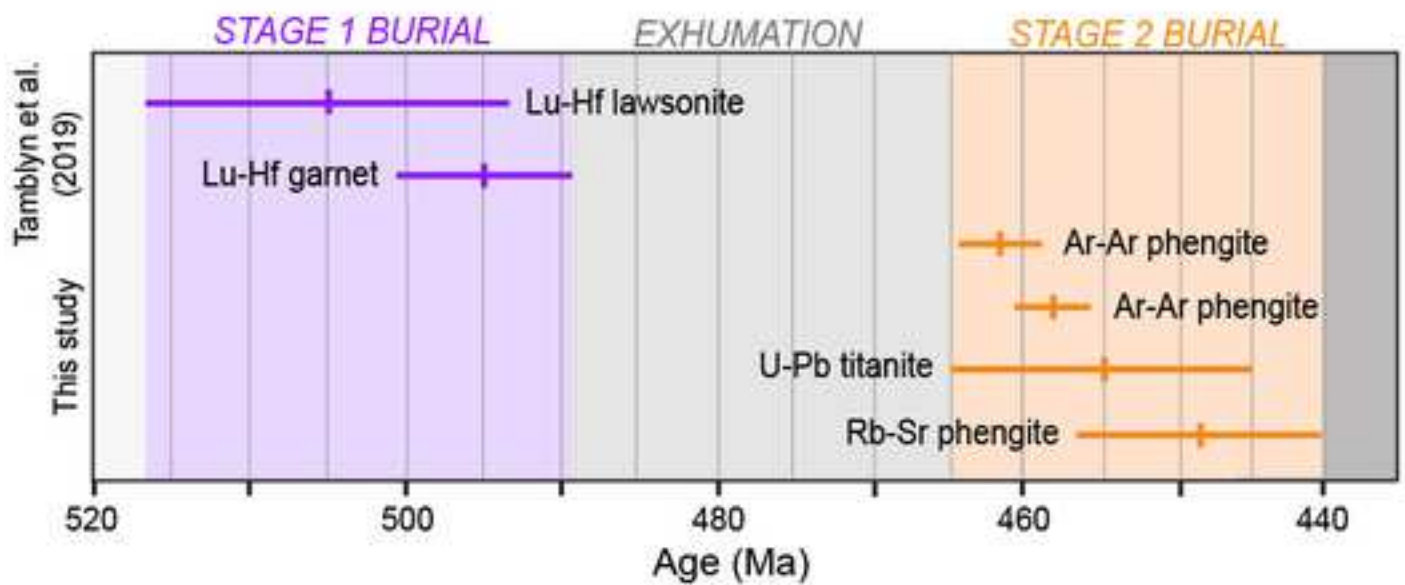
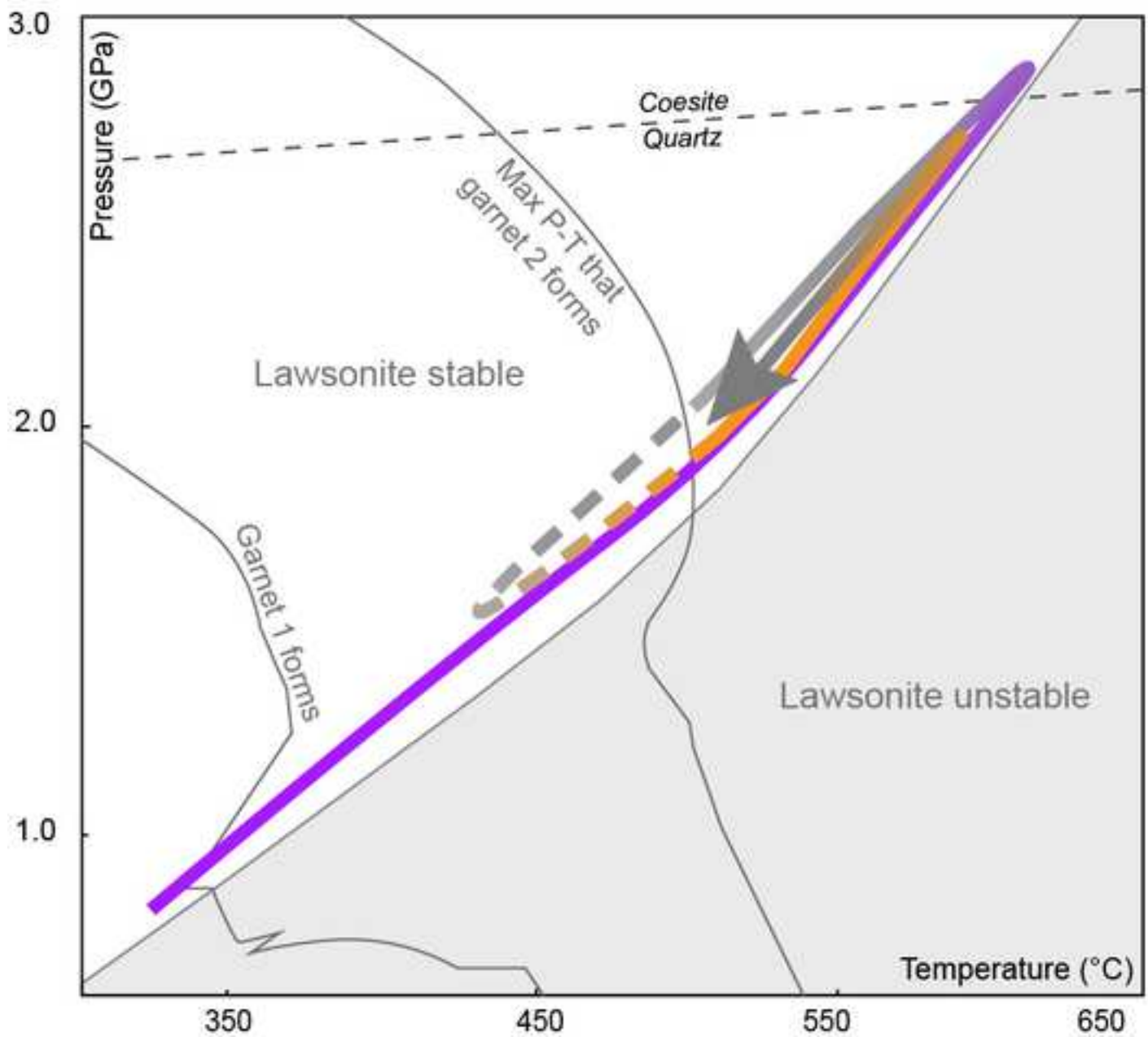


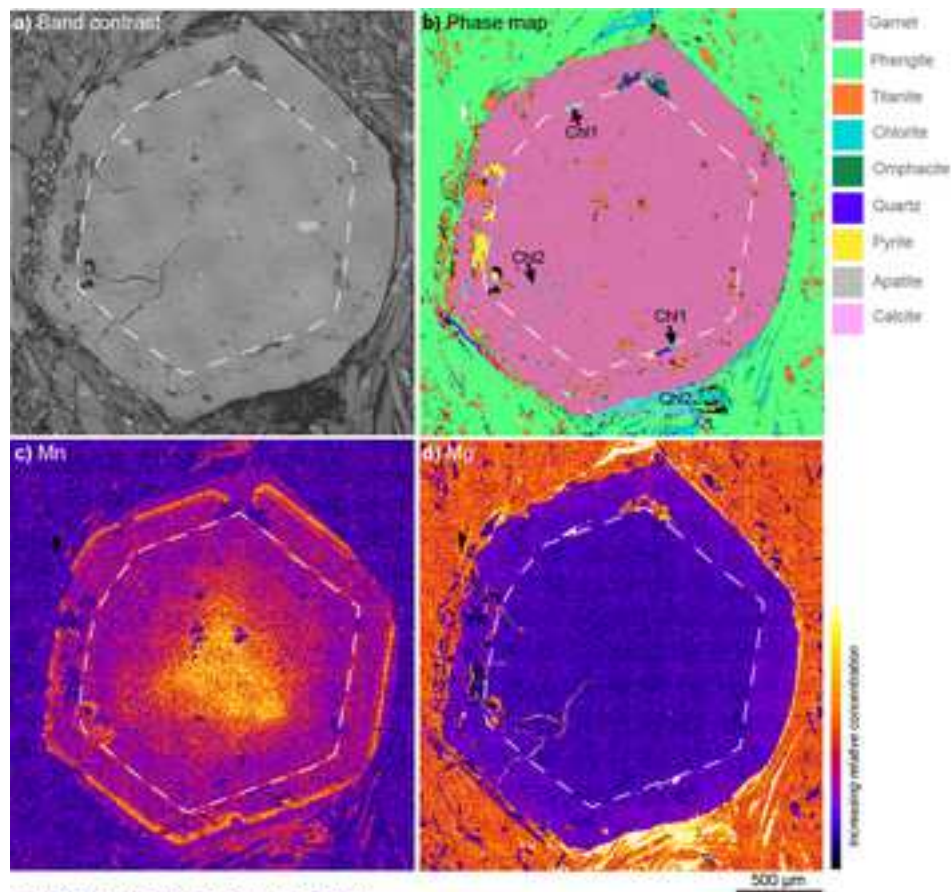
Rb



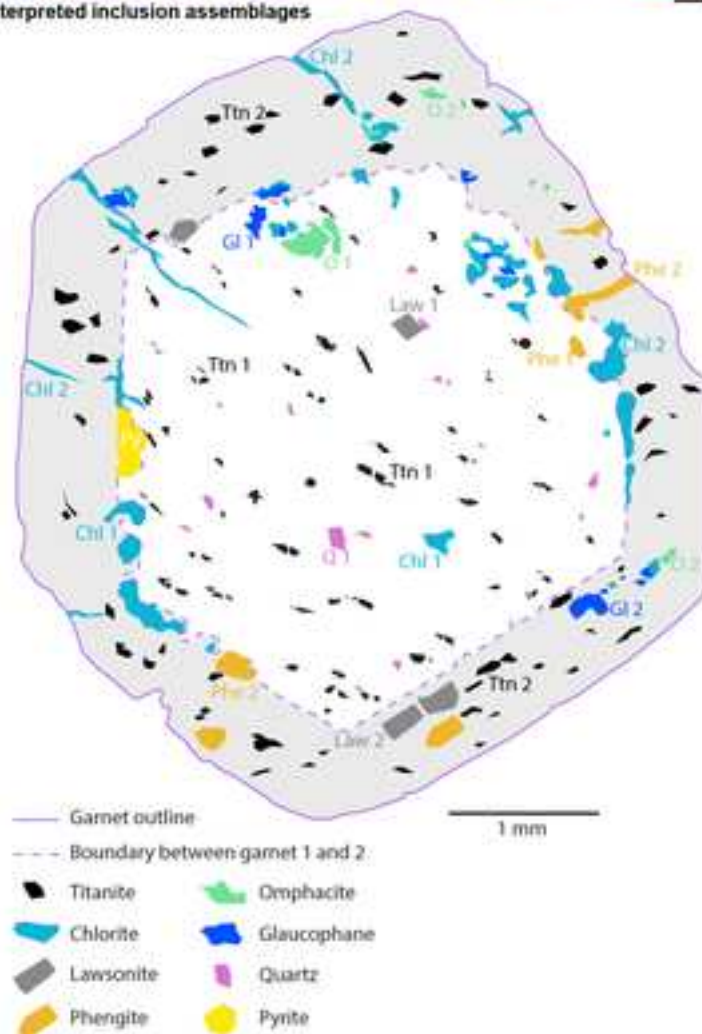
Sr

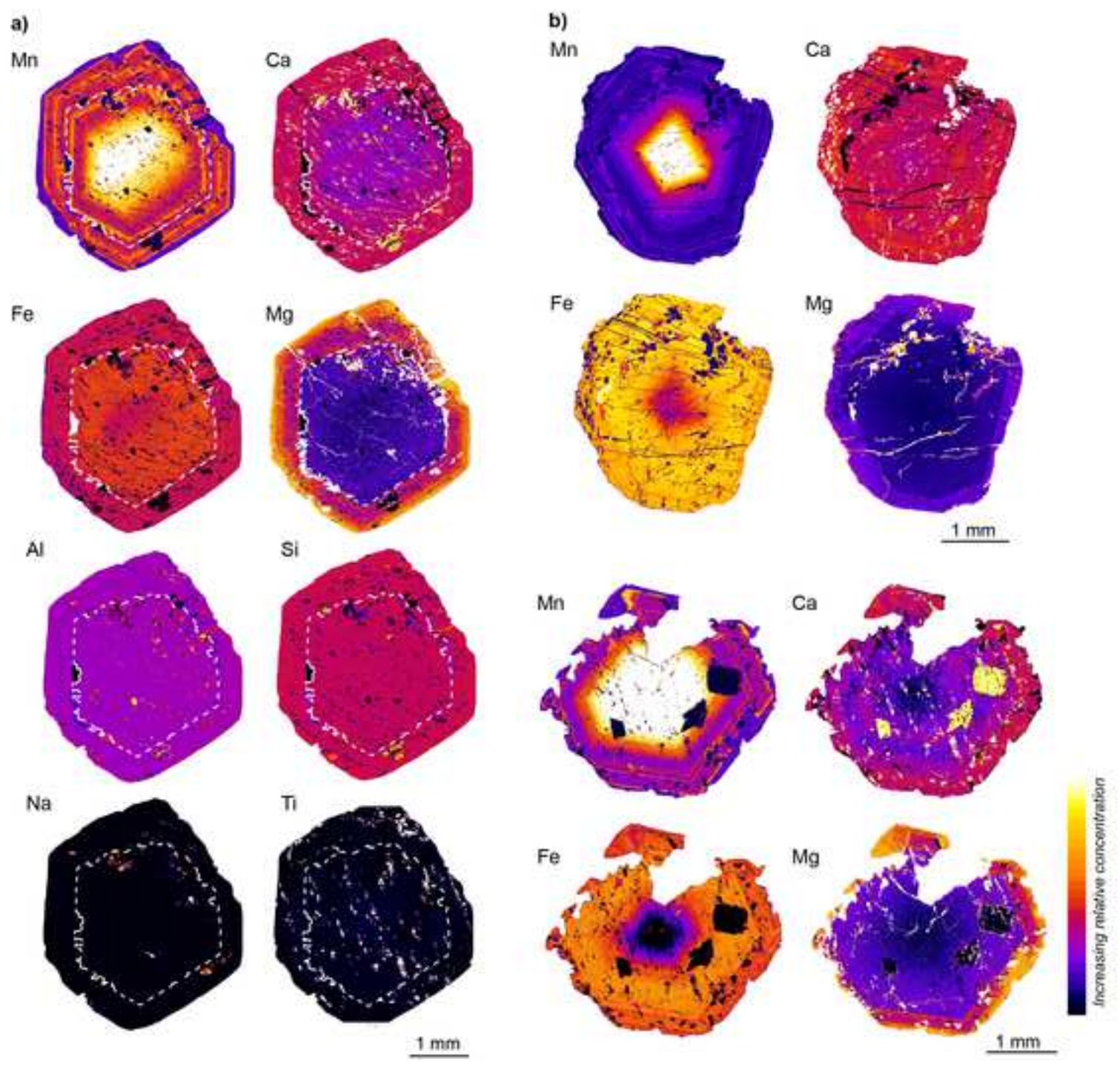


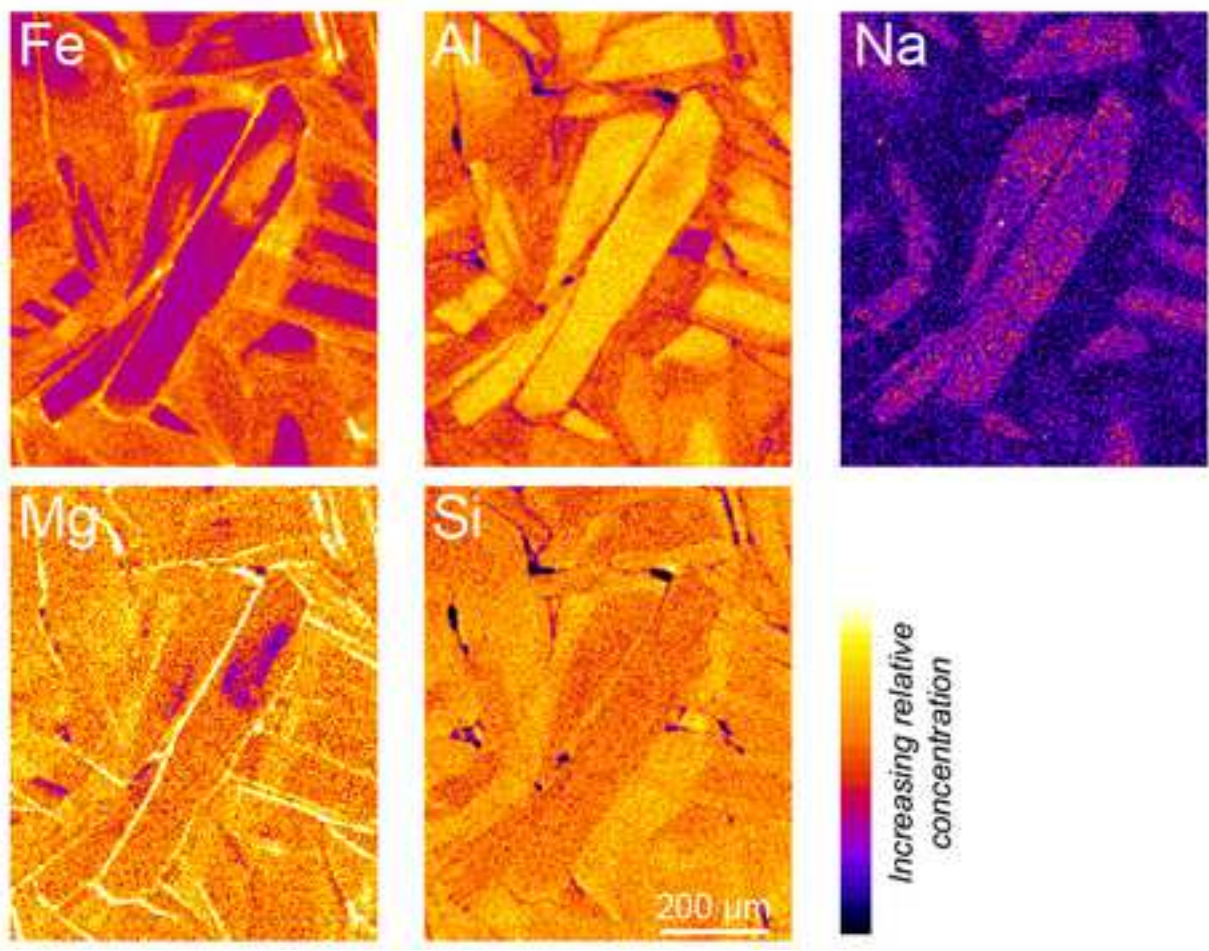
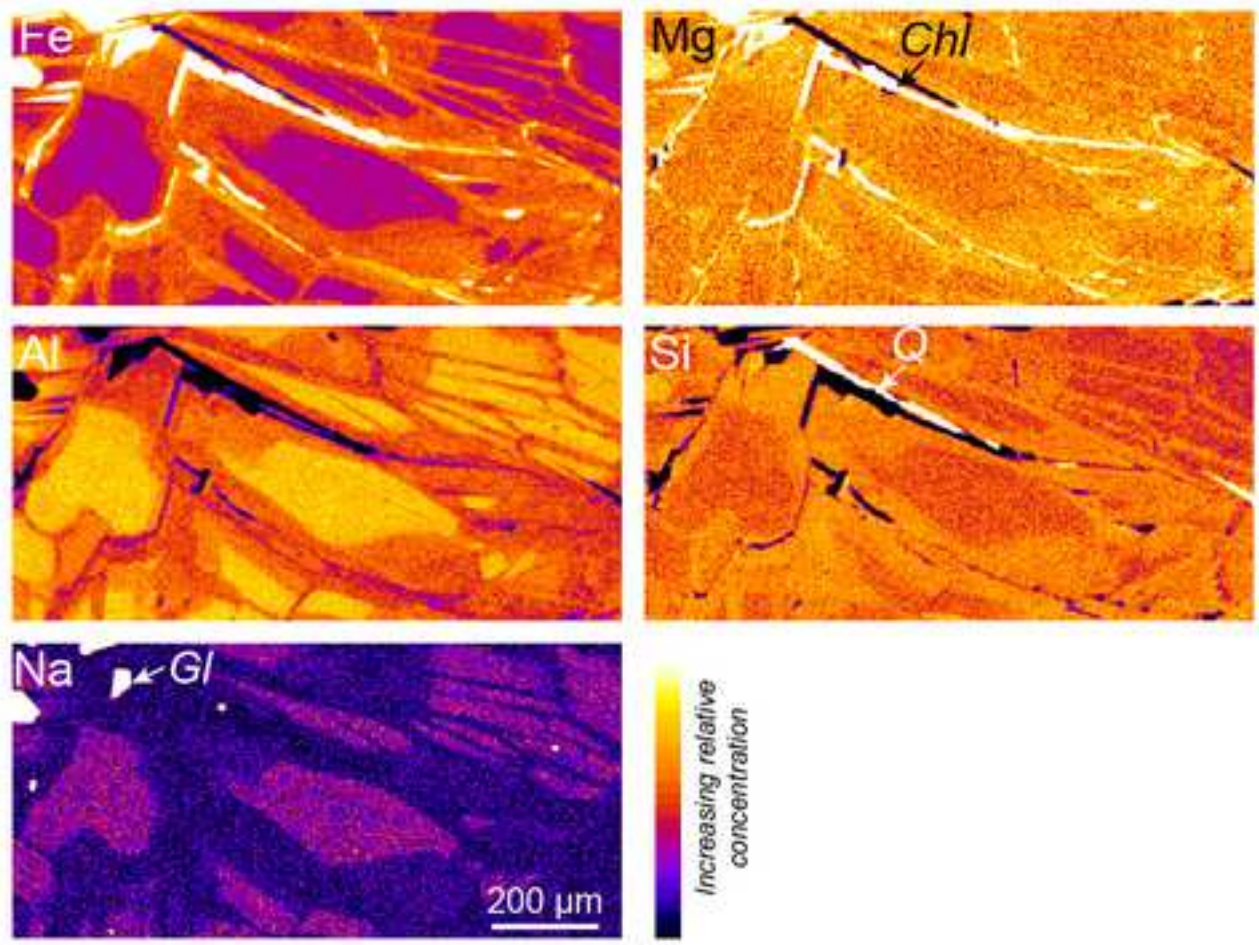


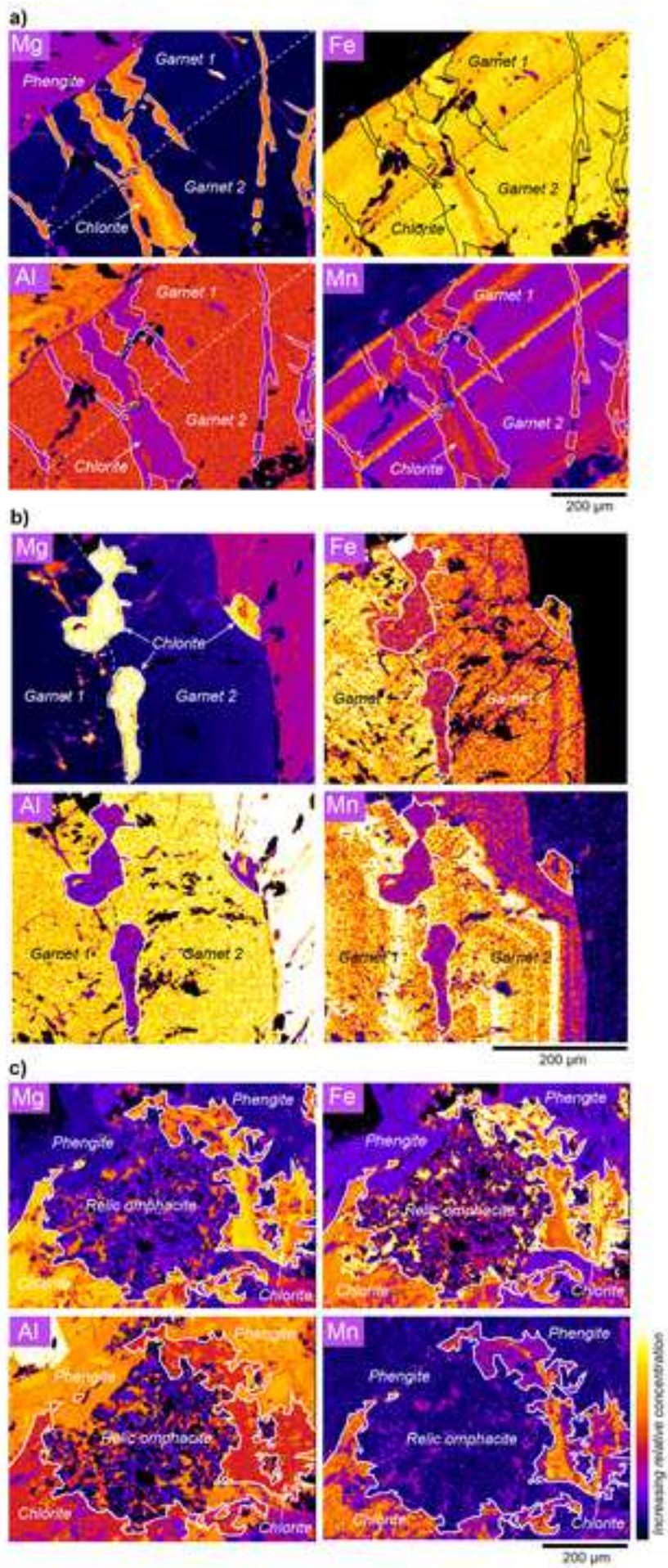


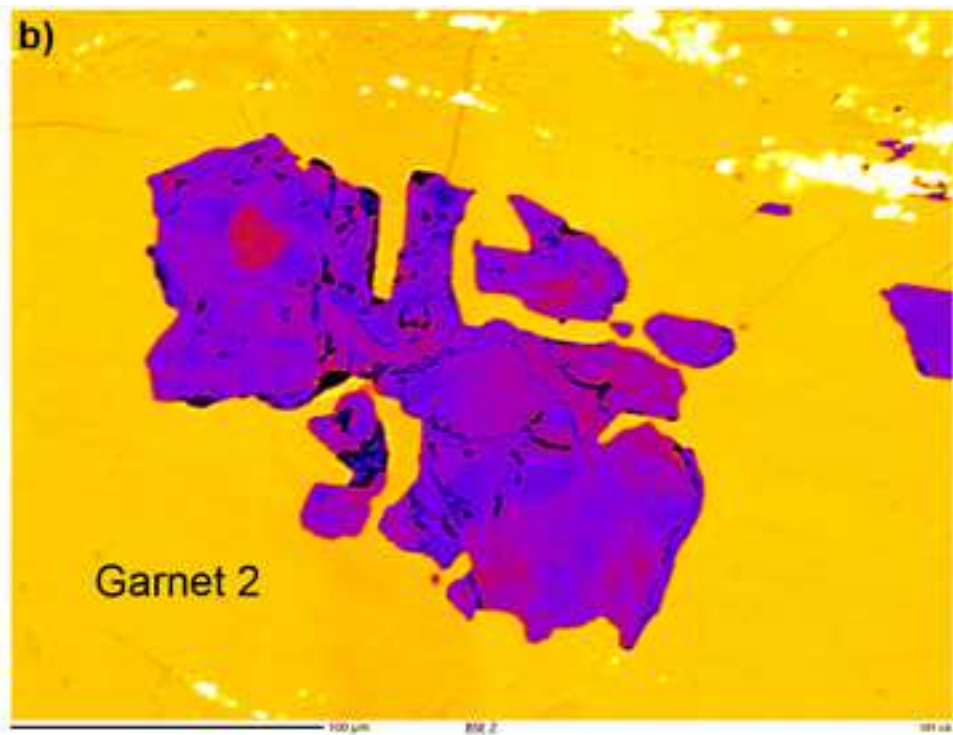
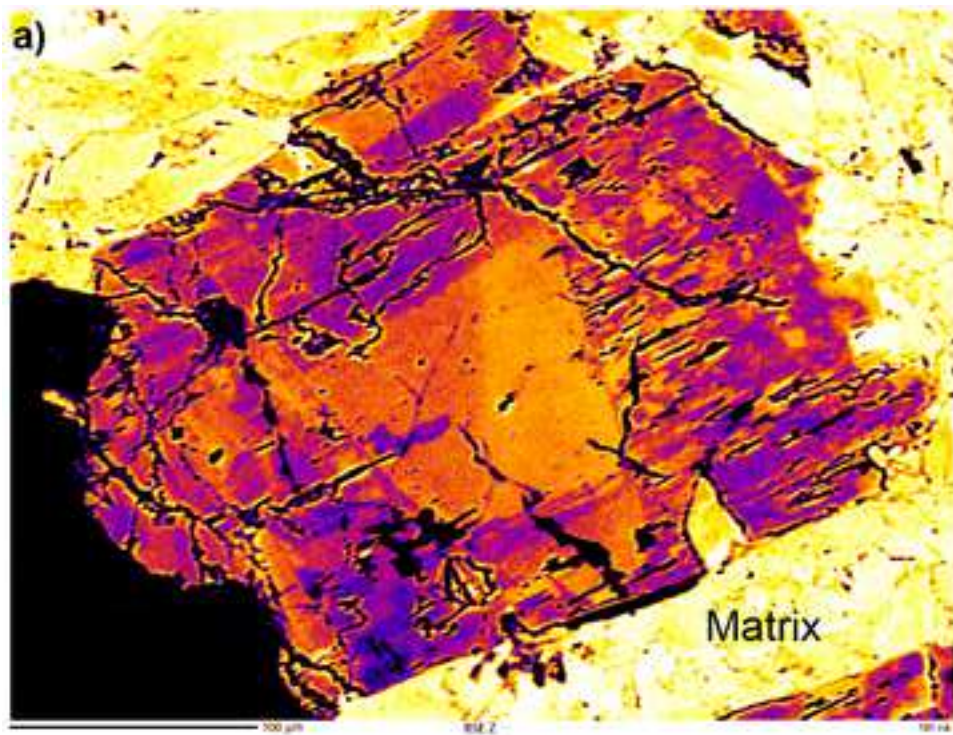
e) Interpreted inclusion assemblages

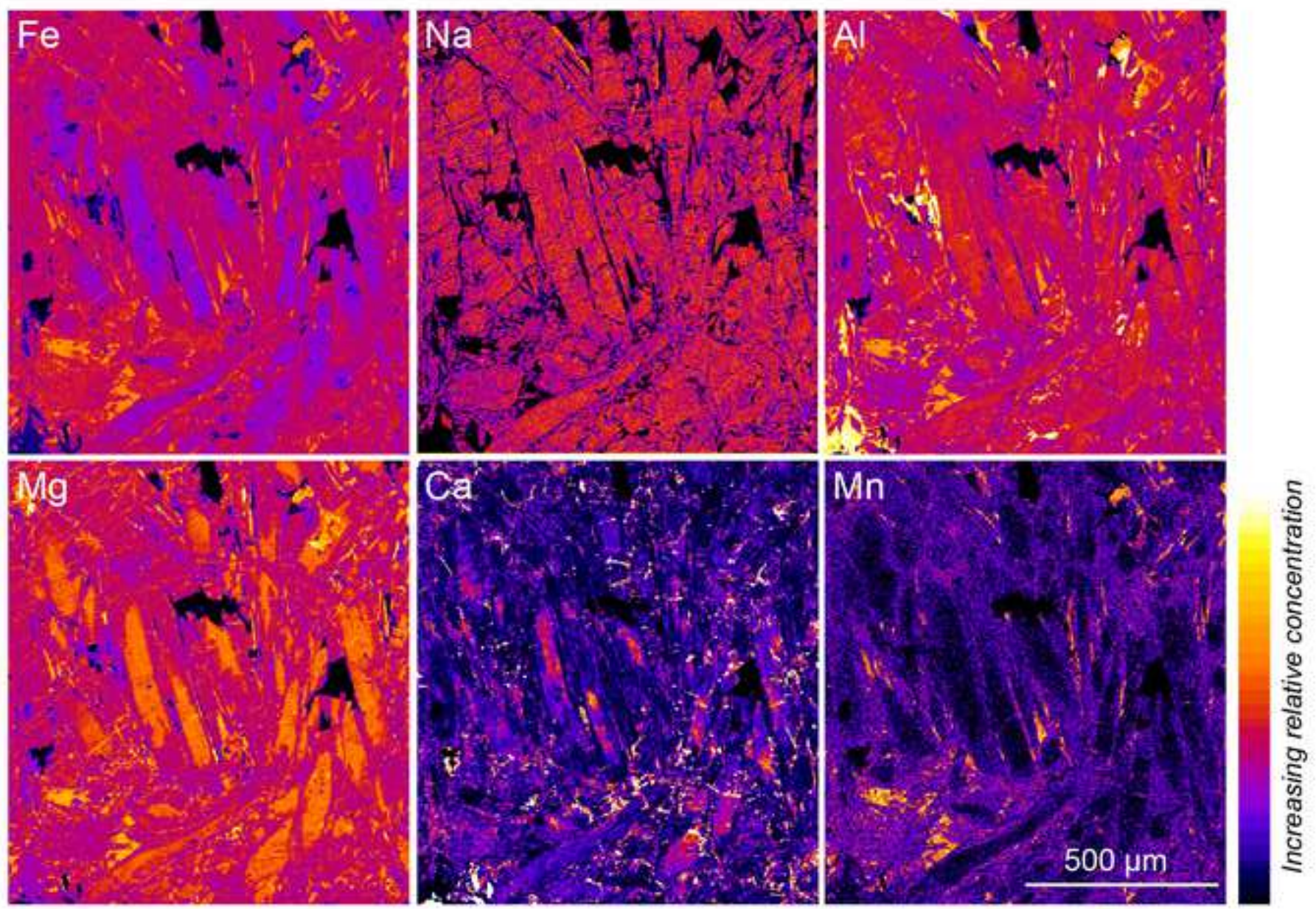












[Click here to view linked References](#)

Supplementary File 1 and supplementary figure captions:

Phase mapping methods

To identify inclusions assemblages in garnet, phase maps were constructed in the Tescan Integrated Mineral Analyser (TIMA) software using data collected on a Tescan Mira3 TIMA with four PulsTor SDD X-ray detectors at the John de Laeter Center, Curtin University. Analysis was conducted in dot-mapping mode with 1 μm BSE pixel spacing. EDS analyses of 1000 counts were acquired at a regular spacing of 5 μm , and additionally at every change in BSE contrast. TIMA software was used to compare BSE intensity and EDS peaks to a custom mineral reference library and automatically classify individual mineral grains. Analytical conditions were an accelerating voltage of 25 kV, beam intensity of 19, probe current of 5.48 nA, spot size of 80 nm, and a working distance of 15 mm.

EBSD map data were collected using a Tescan Mira3 VP-FESEM with Oxford Instruments X-Max 150 SDD X-ray detector, Symmetry EBSD detector and Aztec Synergy software at the John de Laeter Center, Curtin University. Analytical conditions were an accelerating voltage of 20 kV, beam intensity of 18, and working distance of 25 mm. Stage tilt was 70° and step size was 1.22 μm . The EBSD camera was set to binning mode “Speed 1”, camera exposure time was 10 ms, and the camera gain was 2. Auto background correction was used with a Hough Resolution of 40, band detection mode was “Centers”, number of band detected was 11, and indexing mode was “Optimized - TDK”. Band contrast and EDS maps were exported from Aztec and EDS maps were colour scaled in ImageJ.

Extended phase equilibrium modelling methods

The phase equilibria model was calculated using THERMOCALC (TC340i, Powell and Holland, 1988; Holland and Powell, 2011) using the internally-consistent thermodynamic dataset ‘ds5’ (filename tc-ds55.txt; November 2003 updated version of the Holland & Powell, 1998 data set) and activity–composition ($a-x$) models (Supp. Table 2; Holland and Powell, 1988; Holland and

Powell, 2003; White et al., 2007; Green et al., 2007; Holland and Powell, 2011; Diener et al., 2012) in the chemical system NCKFMASHO. The latest thermodynamic dataset ds62 (Green et al., 2016) was not used, to allow direct comparison with the phase equilibria models of Tamblyn et al. (2019a). The Mn-rich interiors of prograde-zoned garnet were not included in the calculated local rock composition for the stage 2 mineral assemblage, so Mn was not considered in the modelled system. Ti was also not considered, due to limitations in modelling the stability of titanite at high pressure. Titanite has been reported to be the stable Ti-bearing phase rather than rutile in systems due to the low activity of CO₂, or minor amounts of Al and Fe³⁺ in its crystal lattice (Enami et al., 1993; Castelli & Rubatto, 2002; Brovarone et al., 2011). As we did not investigate rutile/titanite stability as a function of X_{CO₂}, and the current *a-x* model does not allow Al or Fe³⁺ substitution in titanite, we did not include it in the calculation of bulk compositions or the phase equilibria models. Stilpnomelane was also not predicted in the model as currently there is no *a-x* model available for it.

Water content was handled in two ways. A model for the local rock composition was calculated with water in excess, and a model for the local rock composition was calculated with a set water content, derived from the abundance of hydrous minerals (Table 2; Supp. Table 1). This was done to approximate the two ‘end-members’ of hydration the eclogite may have experienced, with the water content calculated from the abundance of hydrous minerals representing the minimum amount of water available in the rock system. We acknowledge this assumes essentially closed-system behaviour, i.e. does not model water flux into the rock from an external source. As we have no indication that this process occurred, we did not model such behaviour.

Oxidation state (Fe₂O₃) for the sample was constrained from the measured microprobe chemical analyses from each mineral used to calculate the metamorphic local rock composition, by using mineral stoichiometry in the calculation of cations from raw weight % oxides (Table 2; Supp. Table 1; Droop, 1987).

Extended Rb–Sr LA-QQQ-MS methods

Phengite was analysed in-situ for Rb and Sr isotopes and major and trace elements using an ESI 213 NWR (TwoVol2) laser ablation system with an attached Agilent 8800QQQ ICP-MS/MS in the Microgeochemistry Laboratory at the University of Gothenburg, Sweden, following the methods of Zack & Hogmalm (2016) and Hogmalm et al. (2017). Laser parameters were a fluence of $\sim 6 \text{ Jcm}^{-2}$ and a frequency of 10 Hz. Phengite was analysed with a spot size of 40 μm , both perpendicular and parallel to cleavage. Titanite was also analysed to obtain initial $^{87}\text{Sr}/^{86}\text{Sr}$ ratios, with a spot size of 50 μm . The ICP-MS/MS allows separating $^{87}\text{Sr}^+$ from $^{87}\text{Rb}^+$ where Sr^+ reacts with a reaction gas (here N_2O) to form SrO^+ while Rb^+ does not react. Complete separation is achieved by first allowing only one specific M/Z through the first quadrupole (Q1) into the reaction cell and then collect the reacted ion through the second quadrupole (Q2). In detail, to measure ^{86}Sr , Q1 is set to M/Z 86 and Q2 to M/Z 102, while for ^{87}Sr , Q1 is 87 and Q2 is 103. Since not all Sr reacts with N_2O (only about 80%; Hogmalm et al., 2017), ^{87}Rb cannot be analysed interference-free. Instead, ^{85}Rb can be used as a proxy for ^{87}Rb , as $^{87}\text{Rb}/^{85}\text{Rb}$ can be assumed to be constant on Earth within the precisions required for this approach. As Rb^+ does not react with N_2O , Q1 is set to M/Z 85 and Q2 is set to M/Z 85 as well. A range of other isotopes were collected during each analysis together with ^{85}Rb , ^{86}Sr and ^{87}Sr in order to detect and exclude contamination by other minerals, such as: ^{23}Na , ^{24}Mg , ^{27}Al , ^{28}Si , ^{39}K , ^{43}Ca , ^{48}Ti , ^{55}Mn , ^{56}Fe , ^{89}Y , ^{133}Cs , ^{137}Ba , and ^{140}Ce . Laser parameters chosen were a fluence of $\sim 6 \text{ Jcm}^{-2}$ and a frequency of 10 Hz.

Supplementary Figure captions:

Supplementary Figure 1: Phase map and corresponding images showing an example of inclusion assemblages from garnet porphyroblast in Figure 2d. White dashed line indicates the boundary between garnet 1 and garnet 2. a) Band contrast image, showing that there are no cracks or fractures leading to the minerals included on the boundary of garnet 1 and garnet 2. b) Phase map, showing chlorite 1 trapped at the boundary of garnet 1 and garnet 2, and chlorite 2 cross-cutting the garnet porphyroblast. Phengite, omphacite, titanite, quartz and pyrite are also trapped at the boundary of garnet 1 and garnet 2. c) Mn EDS map of the garnet porphyroblast, showing the boundary between

garnet 1 and garnet 2 but also deflections in the Mn zoning around inclusions, indicating they were trapped during garnet growth. d) Mg EDS map, confirming the high-Mg chlorite grains, and also showing the boundary between garnet 1 and garnet 2. e) Schematic diagram of the inclusion assemblages in garnet, traced from phase maps and EPMA compositional maps (Supp. Fig. 1; 2). Chlorite 1 is from both stage 1 prograde and stage 1 retrograde. See figure 2 for abbreviations.

Supplementary Figure 2: Additional EPMA element maps of garnets from lawsonite eclogite. a) Maps of a different garnet that was used to trace the inclusion assemblages in Figure 4 of the main text. b) Maps of two garnets showing prograde zoning in stage 1 garnet. Stage 2 garnet is evident as rims with elevated X_{Mg} . Multiple embayments can be seen in Mn-rich oscillatory zoning.

Supplementary Figure 3: Additional EPMA maps of phengite from the lawsonite eclogite, showing prograde zoning, defined by increasing Si, Fe and Mg.

Supplementary Figure 4: BSE images of omphacite, showing zoning related to Fe content. a) Coarse omphacite crystal in the matrix. b) Omphacite crystals captured in garnet 2, showing similar zoning to omphacite in the matrix.

Supplementary Figure 5: EPMA maps of chlorite in textural positions throughout the lawsonite eclogite, showing that chlorite composition appears related to the minerals it is forming in association with. Continuous white/black line indicates the boundary of a chlorite crystals. Dotted white/black line indicates the boundary between garnet 1 and garnet 2. a) Zoned chlorite, forming in stage 2 retrograde fractures which cross-cut both garnet 1 and garnet 2. b) Chlorite 1, trapped as inclusions between garnet 1 and garnet 2, and chlorite 2, which is consuming garnet 2. The two different stages of chlorite have different compositions. c) Chlorite 2 forming from the breakdown of omphacite in the matrix. The chlorite zoning is patchy, showing strong differences in composition throughout the maps.

Supplementary Figure 6: EPMA maps of texturally late glaucophane from the lawsonite eclogite, showing retrograde zoning that developed during exhumation following stage 2 burial.

References:

- Brovarone, A. V., Groppo, C., Hetényi, G., Compagnoni, R., & Malavieille, J. (2011). Coexistence of lawsonite-bearing eclogite and blueschist: phase equilibria modelling of Alpine Corsica metabasalts and petrological evolution of subducting slabs. *Journal of metamorphic Geology*, 29(5), 583-600.
- Diener, J., & Powell, R. (2012). Revised activity–composition models for clinopyroxene and amphibole. *Journal of metamorphic Geology*, 30(2), 131-142.
- Droop, G. (1987). A general equation for estimating Fe³⁺ concentrations in ferromagnesian silicates and oxides from microprobe analyses, using stoichiometric criteria. *Mineralogical Magazine*, 51(361), 431-435.
- Enami, M., Suzuki, K., Liou, J., & Bird, D. K. (1993). Al-Fe³⁺ and F-OH substitutions in titanite and constraints on their PT dependence. *European Journal of Mineralogy*, 5(2), 219-231.
- Green, E., Holland, T., & Powell, R. (2007). An order-disorder model for omphacitic pyroxenes in the system jadeite-diopsidehedenbergite-acmite, with applications to eclogitic rocks. *American Mineralogist*, 92(7), 1181-1189.
- Green, E., White, R., Diener, J., Powell, R., Holland, T., & Palin, R. (2016). Activity–composition relations for the calculation of partial melting equilibria in metabasic rocks. *Journal of metamorphic Geology*, 34(9), 845-869.
- Hogmalm, K. J., Zack, T., Karlsson, A. K.-O., Sjöqvist, A. S., & Garbe-Schönberg, D. (2017). In situ Rb–Sr and K–Ca dating by LA-ICP-MS/MS: an evaluation of N₂O and SF₆ as reaction gases. *Journal of Analytical Atomic Spectrometry*, 32(2), 305-313.

- Holland, T., & Powell, R. (1998). An internally consistent thermodynamic data set for phases of petrological interest. *Journal of metamorphic Geology*, *16*(3), 309-343.
- Holland, T., & Powell, R. (2003). Activity–composition relations for phases in petrological calculations: an asymmetric multicomponent formulation. *Contributions to Mineralogy and Petrology*, *145*(4), 492-501.
- Holland, T., & Powell, R. (2011). An improved and extended internally consistent thermodynamic dataset for phases of petrological interest, involving a new equation of state for solids. *Journal of metamorphic Geology*, *29*(3), 333-383.
- Zack, T., & Hogmalm, K. J. (2016). Laser ablation Rb/Sr dating by online chemical separation of Rb and Sr in an oxygen-filled reaction cell. *Chemical Geology*, *437*, 120-133.